

Article

Open Access



Quasi-solid polymer electrolytes with binary and ternary salt mixtures for high-voltage lithium metal batteries

Nicola Boaretto^{1,*} , Oihane Garcia-Calvo² , Mónica Cobos², Asier Fernandez de Añastro¹, Marta Diez Viera¹, Mustafa Al Sammarraie Shakir¹, Simon Lindberg¹ , Rosalia Cid Barreno¹ , G r me Godillot³ , Leif Olav J sang⁴, Andriy Kvasha² , Mar a Mart nez-Iba nez¹ 

¹Centre for Cooperative Research on Alternative Energies CIC energiGUNE, Basque Research and Technology Alliance (BRTA), Vitoria-Gasteiz 01510, Spain.

²CIDETEC, Basque Research and Technology Alliance (BRTA), Donostia-San Sebastian 20014, Spain.

³Arkema, Groupement de Recherches de Lacq, Lacq 64170, France.

⁴Cerpotech, Kvenildmyra 6, Heimdal 7093, Norway.

Correspondence to: Dr. Nicola Boaretto, Centre for Cooperative Research on Alternative Energies CIC energiGUNE, Basque Research and Technology Alliance (BRTA), Alava Technology Park, Albert Einstein 48, Vitoria-Gasteiz 01510, Spain. E-mail: nboaretto@cicenergigune.com

How to cite this article: Boaretto, N.; Garcia-Calvo, O.; Cobos, M.; Fernandez de A astro, A.; Diez Viera, M.; Al Sammarraie Shakir, M.; Lindberg, S.; Cid Barreno, R.; Godillot, G.; J sang, L. O.; Kvasha, A.; Mart nez-Iba nez, M. Quasi-solid polymer electrolytes with binary and ternary salt mixtures for high-voltage lithium metal batteries. *Energy Mater.* **2025**, *5*, 500040. <https://dx.doi.org/10.20517/energymater.2024.203>

Received: 1 Oct 2024 **First Decision:** 13 Nov 2024 **Revised:** 28 Nov 2024 **Accepted:** 2 Dec 2024 **Published:** 24 Jan 2025

Academic Editor: Wei Tang **Copy Editor:** Fangling Lan **Production Editor:** Fangling Lan

Abstract

Quasi-solid polymer electrolytes (QSPEs) are considered a promising alternative to liquid electrolytes for high-voltage lithium metal batteries. Herein, we present their properties and performance supported on polyolefin microporous separators. These QSPEs consist of a poly(vinylidene-fluoride-co-hexafluoropropylene) polymer matrix, ethylene carbonate as a plasticizer, and various lithium salt mixtures, including lithium bis(fluorosulfonyl)imide (LiFSI), lithium bis(oxalate)borate (LiBOB), and LiNO₃ as a solid electrolyte interface-forming additive. They exhibit an ionic conductivity of ca. 1 mS cm⁻¹ at room temperature and excellent resistance against lithium dendrites, attributed to the presence of the tough polyolefin separator. The effect of the lithium salt mixture composition on lithium plating/stripping performance and electrooxidation stability was studied in detail, showing that LiNO₃, while having a clear positive effect on the plating/stripping performance, may also adversely affect the oxidative stability of the electrolyte, accelerating the degradation of the cathode/electrolyte interface. QSPEs with binary LiFSI/LiBOB salt mixtures were tested at room temperature in a LiNi_{0.8}Mn_{0.1}Co_{0.1}O₂||Li monolayer



  The Author(s) 2025. **Open Access** This article is licensed under a Creative Commons Attribution 4.0 International License (<https://creativecommons.org/licenses/by/4.0/>), which permits unrestricted use, sharing, adaptation, distribution and reproduction in any medium or format, for any purpose, even commercially, as long as you give appropriate credit to the original author(s) and the source, provide a link to the Creative Commons license, and indicate if changes were made.



pouch cell with a cathode area capacity of *ca.* 2.5 mAh cm⁻². This cell delivered an initial capacity close to 200 mAh g⁻¹ at C/20, 150 mAh g⁻¹ at C/1, and 80% capacity retention after 100 cycles at 25 °C. The results demonstrate the viability of supported QSPEs, based on poly(vinylidene-fluoride-co-hexafluoropropylene), ethylene carbonate, LiFSI and LiBOB, for application in high-voltage quasi solid-state lithium metal batteries.

Keywords: Lithium metal batteries, gel polymer electrolytes, quasi solid-state electrolytes, high voltage, NMC-811, LiNO₃

INTRODUCTION

Gel polymer electrolytes, or quasi-solid polymer electrolytes (QSPEs), are considered as a promising alternative to commercial organic liquid electrolytes for application in lithium-metal batteries^[1-5]. The basic composition of QSPEs includes a polymer host matrix, possibly crosslinked, one or more lithium salts as charge carriers, and liquid organic solvents (sometimes called plasticizers) to help dissociate the lithium salts and increase the ionic conductivity. In some cases, non-soluble inorganic fillers are also added to improve the mechanical properties (passive fillers)^[6-8] or further increase the Li⁺ transport properties (Li-ion conducting fillers)^[9-12]. Typical polyether-based fully solid polymer electrolytes (SPEs), which do not rely on the addition of solvents, have relatively low ionic conductivity ($\ll 10^{-3}$ S cm⁻¹ at room temperature) and cannot sustain low-temperature operation or cycling at high cathode loading and high C-rates^[13]. QSPEs, on the contrary, exhibit ionic conductivity comparable to that of liquid electrolytes, enabling similar cycling performance^[14]. In addition, many polymer host matrices used in QSPEs, such as poly(vinylidene fluoride) and its copolymers, poly(acrylonitrile), polycarbonates, *etc.*, have higher oxidative stability than poly(ethylene oxide) and other polyethers used in SPEs^[15,16]. Consequently, QSPEs are assuming an increasingly important role, especially in high-voltage lithium metal batteries (HV-LMBs) featuring 4V- and 5V-class cathode active materials. Poly(vinylidene fluoride-co-hexafluoropropylene) (PVDF-HFP) is one of the most widely used polymer matrices for QSPEs^[17-24]. Combined with liquid electrolytes, even in concentrations below 50 wt%, it forms mechanically strong and flexible membranes with high ionic conductivity, comparable to liquid electrolytes impregnated in microporous separators. It has high oxidative stability (which in QSPEs is then limited by the liquid electrolyte components)^[16,25], high thermal and mechanical stability (with melting temperature at *ca.* 140 °C), and, depending on the nature of the plasticizers, high fire resistance^[26]. Among the liquid electrolyte solvents used as plasticizers in QSPEs, carbonates provide combined high ionic conductivity and electrochemical stability. While mixtures of linear and cyclic carbonates are routinely used in *in situ* crosslinked QSPEs^[27-29], the high volatility of linear carbonates hinders their use with QSPEs processed by solvent casting routes. On the contrary, cyclic carbonates, such as propylene carbonate (PC)^[30-32], ethylene carbonate (EC)^[33-35], and fluoroethylene carbonate (FEC)^[36], can be used as plasticizers in solvent-processed QSPEs owing to their higher thermal stability. Regarding lithium salts, several options are available, with LiPF₆ being commonly used in combination with mixtures of linear and cyclic carbonates. It provides electrolytes with high ionic conductivity and electro-oxidative stability, but relatively low thermal stability. For SPEs and QSPEs, amide-based salts, such as lithium bis(trifluoromethanesulfonyl)imide (LiTFSI) and lithium bis(fluorosulfonyl)imide (LiFSI), are the most common choices. Besides, other lithium salts are used as additives to protect the electrolyte from electrochemical degradation. Lithium bis(oxalate)borate (LiBOB) and lithium difluoro(oxalate)borate (LiDFOB) are among the most common cathode electrolyte interface (CEI)-forming salt additives^[1,37,38], whereas LiNO₃ is a common solid electrolyte interface (SEI)-forming additive^[39-51]. LiNO₃ is mostly used with ether-based electrolytes in Li-S batteries, in which it forms a multilayer SEI rich in LiN_xO_y and protects the lithium anode from direct contact with the soluble polysulfides^[52]. On the contrary, the low solubility in carbonate-based solvents has limited its use in HV-LMBs. Despite this limitation, the beneficial effects of LiNO₃ in high-voltage batteries have been reported in

several studies. To cite some examples, Zhang *et al.* reported improved performance using LiNO_3 as co-salt in trimethyl phosphate-based QSPEs^[42]. Wang *et al.* used LiNO_3 as the main salt in a triethyl phosphate/fluoroethylene carbonate-based gel polymer electrolyte, formulation showing better performance than the control electrolyte with LiPF_6 ^[53]. Jing *et al.* used *N,N*-dimethylacrylamide to increase the solubility of LiNO_3 in carbonate-based crosslinked gel polymer electrolytes, showing improved cycling performance of $\text{LiNi}_{0.6}\text{Mn}_{0.2}\text{Co}_{0.2}\text{O}_2\|\text{Li}$ cells containing LiNO_3 as co-salt^[46]. Cui *et al.* used LiNO_3 as an additive in poly(ethylene carbonate)-based polymer electrolytes to increase the stability of the SEI^[47,54]. LiNO_3 was also used as a salt additive in low-concentration sulfolane/fluorobenzene-based electrolytes^[48]. In general, LiNO_3 is recognized as a beneficial SEI-forming additive. However, little attention has been paid to its effect on the electro-oxidative stability of electrolytes and the characteristics of the CEI.

Herein, we present the properties and performance of QSPEs supported on a microporous polyolefin separator, composed of PVDF-HFP, EC and two salt mixtures, a binary salt mixture with LiFSI and LiBOB, and a ternary salt mixture with additional LiNO_3 . The attention is in particular on the role of LiNO_3 , as the salt combination LiFSI/LiBOB/ LiNO_3 has been rarely used in polymer electrolytes^[54]. As expected, LiNO_3 greatly improved the Li plating-stripping performance. However, results also indicate a deleterious effect on the oxidative stability of the electrolyte, the cathode charge transfer resistance, and the coulombic efficiency during full cell cycling. This might be due to various factors, such as catalytic activity of LiNO_3 towards electrolyte oxidation, crossover of the LiNO_3 decomposition products from the anode to the cathode, or the interference with the formation of the LiBOB-borne CEI.

Besides, we show that supporting PVDF-HFP-based QSPEs on polyolefin microporous separators has a significant beneficial effect on the resistance against dendrites growth, allowing $\text{Li}\|\text{Li}$ cells cycling for over 1,000 h at a cycled capacity of 2 mAh cm^{-2} and at room temperature. With this improvement, we could cycle NMC-811|QSPE|Li monolayer pouch cells in a practical configuration, featuring a high cathode active material loading (*ca.* 2.5 mAh cm^{-2} and 13 mg cm^{-2}) and a thin lithium metal anode ($\sim 20 \mu\text{m}$ thick). Overall, QSPEs with LiFSI/LiBOB mixture showed excellent performance in NMC-811|Li monolayer pouch cells, at room temperature, with initial discharge capacity of 200 mAh g^{-1} at C/20, 150 mAh g^{-1} at 1C, and 80% capacity retention after 100 cycles. Such cycling results in practical cell configuration indicate that supported QSPEs represent a viable alternative electrolyte for HV-LMBs.

EXPERIMENTAL SECTION

Materials

PVDF-HFP (experimental copolymer grade) was provided by Arkema and dried under vacuum at $100 \text{ }^\circ\text{C}$ before use. LiFSI (Foranext[®]) was provided by Arkema and used without further purification. LiBOB (American Elements, 99.9%) and LiNO_3 (Alfa Aesar, 99%) were dried under vacuum at 60 and $70 \text{ }^\circ\text{C}$, overnight, respectively. Methyl ethyl ketone (MEK, anhydrous, 99.5%, Thermo Scientific) and acetone (anhydrous, 99.8%, max., $0.005\% \text{ H}_2\text{O}$, Thermo Scientific) were used without further purification. PC (99%, $< 10 \text{ ppm H}_2\text{O}$, Sigma Aldrich) and EC (Battery grade, Fujifilm) were used without further purification. Tetra(ethylene glycol)dimethyl ether (99%, Sigma Aldrich) was dried under vacuum at room temperature and stored on molecular sieves. Spray-dried $\text{LiNi}_{0.8}\text{Mn}_{0.1}\text{Co}_{0.1}\text{O}_2$ (NMC-811), used for the full cell tests in coin cells, was kindly provided by Cerpotech. The NMC-811 used for the cycling tests in pouch cells was purchased from Targray. Li sheets laminated on Cu (Li-Cu) were kindly provided by ABEE.

QSPEs preparation

Unsupported quasi-solid electrolytes (QSPEs) for the preliminary study were processed by solvent casting, in an Ar glovebox, by dissolving the PVDF-HFP in acetone and then by adding a solution of lithium salt in a

plasticizer to the PVdF-HFP/acetone solution. The resulting solution was then cast on Mylar® films by a doctor blade and dried at room temperature and reduced pressure (500 mbar) for 16 h. Membranes with thicknesses ranging from 50 to 100 µm and an area of ~200 cm² were produced in this way. With unsupported QSPEs, three plasticizers were tested: tetra(ethylene glycol) dimethyl ether (TEGDME), PC, and EC. LiFSI was used as a lithium salt.

Supported QSPEs were prepared inside a glovebox by solvent casting on a microporous polyolefin separator (Celgard® 2500). MEK was used as a processing solvent. In a typical preparation, the lithium salts (LiFSI, LiBOB, and LiNO₃) were dissolved in EC in the chosen concentration (see Table 1), while 0.4 g of PVdF-HFP was dissolved separately in 6 mL of MEK. Then, 1.6 g of the EC solution was added to the PVdF-HFP/MEK solution, and the resulting mixture was stirred overnight at room temperature. The solution was then cast with a doctor blade on a 10 × 10 cm² Celgard® 2500 sheet, which was placed previously onto a poly(ethylene terephthalate) (Mylar®) foil substrate. The casting was conducted at a speed of 1 mm s⁻¹ and with a blade gap of 300 µm. The casting solvent was finally removed by keeping the membrane under Ar flow overnight at room temperature. Three QSPE compositions were prepared, with LiFSI only, binary LiFSI/LiBOB mixture (in a 4:1 molar ratio), and ternary LiFSI/LiBOB/LiNO₃ mixture (in a 4:1:1 molar ratio). The composition of the prepared QSPEs is reported in Table 1.

QSPE characterization

Thermogravimetric analysis (TGA) was performed with a TGA 209 F1 Libra analyzer (Netzsch). The temperature scans were performed from room temperature up to 600 °C, at a heating rate of 10 °C min⁻¹, and under argon (60 mL min⁻¹). Differential scanning calorimetry (DSC) was performed with a DSC 2500 differential calorimeter (TA Instruments). The scans were conducted in the temperature range between -80 and 100 °C, with a heating rate of 2 °C min⁻¹. The samples were cycled twice between -80 and 100 °C, and the second heating scan was used for the analysis. For the sample preparation, 5-10 mg of each sample was placed in sealed aluminum pans under argon atmosphere.

Ionic conductivity was determined by electrochemical impedance spectroscopy (EIS). The EIS spectra were collected with a Solartron 1260A Impedance/Gain-Phase Analyzer in the frequency range between 32 MHz and 1 Hz (20 points per decade), with a signal amplitude of 10 mV, and in the temperature range between 20 and 80 °C (with 10 °C step). Additionally, the ionic conductivity was measured at 25 °C. For the conductivity measurements, the membranes were placed in coin cells CR2032, with three stainless-steel (SS) plates of 0.5 mm thickness. The temperature was controlled with a Binder KB23 cooling incubator. The ionic conductivity was calculated using:

$$\sigma = \frac{1}{R} \frac{L}{A} \quad (1)$$

where σ is the ionic conductivity, R is the measured resistance, A is the electrode surface area, and L is the membrane thickness. The latter was measured with a digital micrometer after the experiment. The measurement was repeated on three different cells for each composition, and the values of resistance and conductivity used in the analysis are the average values of the three measurements.

The morphology of a QSPE cross-section, obtained by an ion milling technique (Hitachi 4000 Plus), was analyzed by field emission scanning electron microscopy (FESEM, APREO 2 S HiVac FESEM). QSPE samples were transferred between the glovebox, the ion milling and the scanning electron microscope (SEM), under argon atmosphere, with a transfer device. Cross-sectioning was performed at -70 °C with a cryogenic module.

Table 1. Composition of the three QSPEs prepared in this study

	PVdF-HFP/wt%	EC/wt%	LiFSI/wt%	LiBOB/wt%	LiNO ₃ /wt%
QSPE-1	20	70	10	-	-
QSPE-2	20	70	8.0	2.0	-
QSPE-3	20	69.4	7.9	2.0	0.7

The lithium transference number (T^+) was measured on a VMP3 potentiostat (BioLogic), in Li||Li coin cells, at 25 °C. The lithium T^+ was determined by combining a chronoamperometry step with the measurement of the impedance spectra, collected before and after the chronoamperometry step. For the chronoamperometry, a constant voltage of ± 10 mV was applied for a duration of 20 min, and the resulting current was registered with a frequency of 100 Hz during the 30 s, and 1 Hz during the rest of the chronoamperometry. The impedance spectra were collected in the frequency range between 1 MHz and 100 mHz (20 points per decade) and with potential amplitude of 10 mV. For each composition, the experiment was repeated on three cells and six times on each cell, by alternating positive and negative potentiostatic polarization. The cells were allowed to relax for one hour after each chronoamperometric step, and for 10 min after the EIS measurement. The T^+ was then calculated using^[55]:

$$T^+ = \frac{R_{b,0}}{(\Delta V / I_{SS} - R_{int,SS})} \quad (2)$$

where I_{SS} is the initial and steady-state current, ΔV is the applied potential, $R_{int,SS}$ is the interfacial resistance after the chronoamperometric step, and $R_{b,0}$ is the bulk resistance before the chronoamperometry.

The oxidative stability of the three QSPEs was studied, by linear sweep voltammetry (LSV) and floating test, in coin cells with carbon-coated Al foil discs (cc-Al) as working electrodes, and lithium metal electrodes as counter/reference electrodes. LSV scans were carried out at an ultra-low scan rate of 5 $\mu\text{V s}^{-1}$ between the open circuit potential and 5.0 V vs. Li/Li⁺. Floating current tests were conducted in the same cell configuration. First, the cell potential was increased to 3.9 V vs. Li/Li⁺ at 0.1 mV s⁻¹. Then, the potential was increased stepwise up to 5.0 V vs. Li/Li⁺, with step amplitude of 100 mV and step duration of 10 h.

Cathode active material preparation

NMC-811 powder from Cerpotech was produced by spray pyrolysis. In a typical synthesis, an aqueous solution was prepared by dissolving stoichiometric amounts of metal nitrates in distilled water and mixing individual precursor solutions under stirring. The homogeneous solution was atomized by a two-phase nozzle (pressurized air + solution) into a pre-heated rotary furnace (≈ 2 rpm) (Entech Energitechnik AB) under constant air flow, yielding an approximate average residence time of 2 s at 700-1,000 °C. This caused instant vaporization of water and onset of nitrate decomposition, as mixed metal oxide began to form. The collected powders were calcined in alumina crucibles in a tube furnace (Entech) at 850 °C for 6 h under a constant oxygen flow (Praxair 5.0) with heating and cooling rates of 200 °C h⁻¹.

Cathode preparation

The N-Methyl-2-pyrrolidone (Merck)-based slurry, composed of 81.3 wt% of NMC-811 (Cerpotech), 4.5 wt% of C45 carbon black (Imerys) and 14.2 wt% of catholyte, was prepared using a mechanical stirrer (IKA). The catholyte comprised a mixture of PVdF-HFP (Arkema), 1-butyl-1-methylpyrrolidinium bis(trifluoromethylsulfonyl)imide (PYR14TFSI, 99.9%, Solvionic), and LiFSI (Arkema), to promote Li⁺ ionic conductivity within cathode active layer and simultaneously maintain mechanical integrity of the positive electrode. The homogenized slurry was cast over a carbon-coated aluminum current collector with a

thickness of 20 μm by an automatic film applicator 1137 (SHEEN Instruments). The electrode was dried in a convection oven at 110 $^{\circ}\text{C}$ for 15 min. The dried electrode with a final loading of 13 $\text{mg}_{\text{NMC-811}} \text{cm}^{-2}$ was compressed by a laboratory hydraulic roll calender (DPM Solutions, Canada) to $3.0 \pm 0.1 \text{ g cm}^{-3}$ density and finally dried under dynamic vacuum at 120 $^{\circ}\text{C}$ for 16 h in the dry room. NMC-811||Li-Cu coin cells were fabricated with the spray-dried NMC-811 cathode active material.

Owing to the limited availability of the spray-dried active material, NMC-811||Li-Cu single-layer pouch cells were fabricated with commercial NMC-811 (T81RX, Targray). Firstly, a 1 kg slurry batch with the abovementioned formulation was prepared in a dry room (dew point of -40 $^{\circ}\text{C}$) using a mechanical mixer. Then, the one-sided positive electrode coating of a carbon-coated 20 μm aluminum current collector (Gelon) was carried out using a modified base-coater pilot narrow width machine (up to 300 mm) with a dryer comprising three separated 1-meter-long zones (COATEMA). Finally, the cathode application with confirmed loading level (2.5 mAh cm^{-2} , 13.8 $\text{mg}_{\text{NMC-811}} \text{cm}^{-2}$) was calendered at room temperature until reaching an electrode density of $3.0 \pm 0.1 \text{ g cm}^{-3}$ using roll press LDHY400-N45 (Naknor). Before pouch cell assembly, notched cathodes with dimensions of 50 \times 60 mm^2 were dried under dynamic vacuum at 120 $^{\circ}\text{C}$ for 16 h in a dry room (dew point of -50 $^{\circ}\text{C}$). Lithium metal anodes with a thickness of 50 μm (Albemarle) and dimensions of 50 \times 60 mm^2 were manually cut inside a dry room (dew point of -50 $^{\circ}\text{C}$) right before pouch cell assembly.

Cell assembly and testing

All coin cells (Hohsen Corp.) were assembled in an Ar.-filled glovebox (MBraun) with H_2O and O_2 concentrations below 1 ppm, and with a manual coin cell crimper (Hohsen Corp.).

The plating/stripping performance of QSPEs was tested at 25 $^{\circ}\text{C}$, in Li||Li symmetric coin cells with Li electrodes supported on Cu sheets (14 mm-diameter, ABEE). The cells were cycled galvanostatically with a Neware battery tester at 25 $^{\circ}\text{C}$ and at a fixed capacity of 2 mAh cm^{-2} . Five cycles were performed at 0.2 mA cm^{-2} (C/10), followed by 5 cycles at 0.4 mA cm^{-2} (C/5), 0.67 mA cm^{-2} (C/3), 1 mA cm^{-2} (C/2) and 2 mA cm^{-2} (C/1). Thereafter, the cells were cycled at C/10 until failure.

Plating/stripping coulombic efficiency was determined by cycling Cu||Li cells, with 500 μm -thick Li discs (14 mm diameter) as counter electrodes and Cu discs (16 mm diameter) as working electrodes. Thick Li foil was used to avoid any effect due to depletion of the negative electrode, as the study of the deposition and stripping process on the Cu foil was the target of this test. Tests were conducted with a Neware battery tester at 25 $^{\circ}\text{C}$. Firstly, a current of -0.1 mA cm^{-2} was applied for 20 h, followed by application of a positive current with the same amplitude, until a cutoff voltage of 0.2 V was reached. This full plating/stripping cycle was performed twice and served as a conditioning cycle, to establish a stable SEI on the Cu foil surface. Then, a plating half cycle was performed, with the same conditions described above, with the aim of creating a Li reservoir on the Cu foil. Thus, this Li reservoir corresponds to an area capacity of 2 mAh cm^{-2} . Thereafter, fifty short plating/stripping cycles were performed, with a current density of 0.1 mA cm^{-2} and a half cycle time of 2 h. In these short cycles, a capacity of 0.2 mAh cm^{-2} is cycled back and forth. Finally, a positive current of 0.1 mA cm^{-2} was applied, until the cutoff voltage of +0.2 V was reached. The coulombic efficiency of the first 2 cycles was calculated by the ratio of the stripping capacity to the fixed plated capacity. In addition, the average coulombic efficiency during the intermediate short cycles was calculated by^[56]:

$$C.E. = \frac{(nQ_C + Q_S)}{(nQ_C + Q_T)} \quad (3)$$

where n is the number of short cycles performed, Q_c is the capacity cycled in the short cycles (0.2 mAh cm^{-2}), Q_s is the capacity of the final stripping half cycle, and Q_T is the total plated capacity in the Li reservoir (2 mAh cm^{-2}).

NMC-811||Li-Cu coin cells were prepared with NMC-811 electrode discs (12 mm diameter) and Li-Cu discs (14 mm diameter) as positive and negative electrodes, respectively. The top side of the QSPE during casting faced the positive electrode in the full cells. Galvanostatic C-rate and cyclability tests of NMC-811||Li-Cu coin cells were conducted with a Neware battery tester. During the C-rate capability test, the cells were cycled between 3.0 and 4.3 V. Two cycles were performed at C/20 (calculated on a nominal capacity of $170 \text{ mAh g}_{\text{NMC-811}}^{-1}$), followed by 5 cycles at each of the following C-rates: C/10, C/5, C/3, C/2, and C/1. Thereafter, the cells were further cycled at C/10 until failure. Cyclability tests and EIS were carried out in coin cells with a BT-Lab battery tester. In these tests, the cells were cycled between 3.0 and 4.3 V at C/20 (2 cycles) and at C/10 (100 cycles). EIS spectra were collected at the end of discharge (EoD) every 5 cycles. EIS tests upon cycling in three-electrode cell configuration were carried out with ECC-PAT-core cells (EL-CELL[®]), with a VMP3 potentiostat (BioLogic). Cells were cycled between 3.0 and 4.3 V at C/50 (2 cycles) and C/20 (30 cycles). EIS spectra were collected both at the end of charge (EoC) and discharge. All full cell tests were performed at $25 \text{ }^\circ\text{C}$.

Single-layer pouch cells were manually assembled by stacking alternate layers of the positive electrode, QSPE film and negative electrode. When the cell stack was assembled, nickel and aluminum tabs (MTI Corp.) were ultrasonically welded to negative and positive electrode tabs, respectively. Finally, the solid-state battery was sealed under vacuum in an aluminum laminated pouch bag. The entire assembly was conducted in a dry room with a dew point of $-50 \text{ }^\circ\text{C}$. Before cycling, the freshly fabricated solid-state battery was placed between two metal plates, clamped with a torque of 0.3 N m^{-1} , and kept for three hours at $25 \text{ }^\circ\text{C}$ to ensure the formation of intimate contacts between both electrodes and the solid electrolyte. Finally, the assembled solid-state pouch cells were cycled at $25 \pm 1 \text{ }^\circ\text{C}$ by BaSyTec cell test system, in accordance with the protocol described in Table 2.

X-ray photoelectron spectroscopy analysis

The surface chemistry of Li deposits on Cu under striping/plating experiments was analyzed by X-ray photoelectron spectroscopy (XPS) using a Phoibos 150 XPS spectrometer (SPECS GmbH) installed in an ultrahigh vacuum (UHV) chamber with a base pressure below $5 \times 10^{-10} \text{ mbar}$. Samples were transferred in an argon-filled air-tight container from the glove box to the instrument after cell disassembly. Spectra were collected in Fixed Analyzer Transmission mode with $\sim 2 \text{ mm}$ field of view on the sample using a non-monochromatic Mg anode source ($h\nu = 1253.6 \text{ eV}$). $E_{\text{step}} = 0.5 \text{ eV}$ and $E_{\text{pass}} = 90 \text{ eV}$ were employed for the survey spectra and $E_{\text{step}} = 0.1 \text{ eV}$ and $E_{\text{pass}} = 30 \text{ eV}$ for the high-resolution regions. The atomic surface species were quantified using tabulated Scofield cross sections, applying corrections to the integrated intensity considering the energy-dependent analyzer transmission and the variations in the effective attenuation lengths (EAL) of the collected photoelectrons depending on their kinetic energies using the analytical expression proposed by Seah^[57]. Data analysis was carried out using CASA XPS software^[58]. The binding energy scale was calibrated by referencing the aliphatic carbon at 285 eV . The inelastically scattered photoelectron background was simulated by a Shirley function, and Voigt profiles (30% Gaussian, 70% Lorentzian) were employed as line shapes for the photoelectron peaks.

RESULTS AND DISCUSSION

QSPE characterization

The chosen composition of the QSPEs results from previous optimization work, aimed at achieving the best

Table 2. Cycling protocol for single layer pouch cells with nominal capacity 0.08 Ah, and cathode with loading of 2.5 mAh cm⁻²

Step	Cycling conditions (25 °C)
Formation cycle	Charge/discharge current: C/20; Cycling interval: 3.0-4.3 V
Discharge capacity rate	Charge current: C/10; Charge current cut off: C/20 Discharge currents (5 cycles each): C/10, C/5, C/3, C/2, 1C, C/3, C/5 Cycling interval: 3.0-4.3 V
Long-term cycling	Charge/discharge current: C/10; Cycling interval: 3.0-4.3 V Capacity cutoff: 80% of discharge capacity (1st value at C/10)

compromise between mechanical and transport properties, oxidative stability, and plating stripping performance, to allow room-temperature operation in HV-LMBs. The PVdF-HFP content was optimized to give the highest ionic conductivity while retaining mechanical integrity and was finally set to 20 wt%. At lower PVdF-HFP contents, no self-standing membranes could be obtained. Initially, unsupported membranes were prepared and tested. For these initial trials, acetone was used as a processing solvent. Several lithium salt solvents (plasticizers) were tested, including PC, tetra(ethylene glycol)dimethyl ether, and EC, among which EC gave the best results in terms of ionic conductivity [Supplementary Figure 1] and plating/stripping performance in Li||Li symmetric cells [Supplementary Figure 2]. When tested with thin Li-Cu electrodes, the membranes allowed plating/stripping up to a capacity of 1 mAh cm⁻² [Supplementary Figure 3] but underwent rapid short circuit after a few cycles at a plated/stripped capacity of 2 mAh cm⁻² and at a C-rate of C/10 (0.2 mA cm⁻², results not shown). Consequently, a microporous separator was added to increase the resistance against dendrites penetration and to allow cycling in full cells at high cathode active material loading (2-3 mAh cm⁻²), necessary to achieve a high energy density at the cell level. The focus of this study is on further optimizing the QSPE composition and examining the effect of the salt mixture composition, particularly LiNO₃, on cell performance. Three supported QSPEs were prepared and characterized, containing LiFSI as a unique salt (QSPE-1), a binary mixture of LiFSI and LiBOB in a 4:1 molar ratio (QSPE-2) and a ternary salt mixture of LiFSI, LiBOB, and LiNO₃, in a 4:1:1 molar ratio (QSPE-3). The exact composition of the three QSPEs is reported in Table 1. The QSPEs were prepared by solvent casting on a microporous polyolefin separator (Celgard 2500), resulting in homogeneous, translucent membranes with a thickness of *ca.* 60-80 μm. Having a high thickness was necessary to ensure complete penetration of the QSPE into the separator and, additionally, to ensure good contact with both the anode and the cathode. The excess QSPE on the cathode side may help compensate for possible residual porosity in the catholyte phase and thus reduce the interfacial resistance between the cathode layer and the QSPE. The relatively high thickness of the supported QSPEs might obviously affect the cell energy density. However, the QSPE thickness might be reduced by optimizing the casting conditions or using polyolefin separators with a reduced thickness. For instance, by using a (commercially available) 15 μm thick separator, final thicknesses below 50 μm may be easily achieved.

The preparation process of the supported QSPEs was slightly modified to make it more compatible with a possible scale-up to a continuous roll-to-roll process. First, the processing solvent was changed, from acetone to MEK, which has a lower evaporation rate. Additionally, the drying method was altered from drying under static at 500 mbar at room temperature to drying under Ar flow. As in the previous case, this change was necessary to replicate the processing conditions in a roll-to-roll coating line, where vacuum cannot be applied.

Cross-section SEM images of a QSPE membrane [Supplementary Figure 4] show the good adhesion of the overlaying QSPE layer on the infiltrated microporous separator, while porosity formation was observed during SEM acquisition, owing to EC evaporation under high vacuum. The presence of residual MEK was controlled by Fourier transform infrared spectroscopy (FTIR) and nuclear magnetic resonance (NMR). No

residual MEK was detected by either NMR or FTIR. In the proton NMR spectra [Figure 1A], MEK gives an intense signal at 2.1 ppm, which was not detected in the spectra of the QSPEs. The most intense peak in the QSPE spectra is due to EC at *ca.* 5 ppm. FTIR spectra of QSPE-2, processed either with acetone or MEK, are reported in Figure 1B. The spectra are similar, and most importantly, the intense C=O stretching peak of MEK at 1,718 cm^{-1} was not observed, confirming absence of residual process solvents. In the carbonyl stretching region, only the doublet related to EC, at 1,774 and 1,801 cm^{-1} , is visible in both spectra.

The thermal properties of the three QSPEs were analyzed by TGA and DSC. The TGA profiles [Figure 1C and D] show a slow mass loss up to at least 100 °C, attributed to EC evaporation, followed by a rapid mass loss at *ca.* 150 °C, which is caused by faster EC evaporation and possibly salt degradation. A final mass loss is observed at 500 °C, corresponding to the thermal degradation of the polymer matrix. The initial mass loss is slightly faster for QSPE-1, for which the 95 wt% threshold is reached at 97 °C. For comparison, the same threshold is reached at 137 and 122 °C in QSPE-2 and QSPE-3, respectively. The mass loss of the three QSPEs at 300 °C corresponds approximately to the content of EC, namely 60 wt%. The DSC profiles [Figure 1E] show some differences between the three QSPEs. The QSPE-1 has a glass transition temperature (T_g) of *ca.* -72 °C and two melting transitions, at -25 and 22 °C, preceded by a weak crystallization at -50 °C, with enthalpy of *ca.* 1 J g^{-1} . The SPEs with binary and ternary salt mixtures, QSPE-2 and QSPE-3, exhibit T_g of -67 and -62 °C, respectively. Both show a melting transition at 20 °C, which is attributed to the melting of the EC. The different crystallization/melting behaviors with the binary and ternary salt mixtures possibly arise from the increased disorder, caused by the presence of various anions, whereas the increase of the T_g might indicate a lower mobility of BOB^- and NO_3^- , with respect to FSI^- . Nonetheless, the ionic conductivity of the three QSPEs is remarkably similar, slightly higher than 1 mS cm^{-1} at room temperature and $\sim 3 \text{ mS cm}^{-1}$ at 80 °C [Figure 1F, Table 3]. Interestingly, the ionic conductivity is close to that of unsupported QSPEs [Supplementary Figure 1B], although the addition of the separator, with a 55% porosity, was expected to lower the ionic conductivity. This is probably due to the large thickness of the QSPEs, dampening the effect of the microporous separator, which has a thickness of 25 μm . Altogether, this conductivity is expected to be high enough to allow cell cycling at room temperature. The lithium-ion T^+ at room temperature was determined by the potentiostatic polarization method and is also reported in Table 3. T^+ is close to 0.1 and increases slightly from QSPE-1 (0.09 ± 0.01) to QSPE-3 (0.14 ± 0.01). The low value of T^+ indicates that most of the ionic conductivity is due to the motion of the anions and is attributed to the strong coordination of Li^+ by the EC molecules. The slight increase observed from QSPE-1 to QSPE-3 is attributed to the partial substitution of FSI^- with less mobile BOB^- and NO_3^- anions. Some representative chronoamperometric profiles and correspondent EIS spectra are reported in Supplementary Figure 5. In the chronoamperometry profiles, the steady state is reached within a few seconds (less than one minute in most cases), owing to the high ionic conductivity of the QSPEs. Additionally, the EIS spectra were used to estimate the Li|QSPE area-normalized interface resistance (R_{int}^* , Table 3). This was calculated by multiplying R_{int}^* by the electrode area and dividing the resulting value by two (thus accounting for the presence of two Li electrodes). In this case, the effect of the salt mixture composition is significant, with R_{int}^* decreasing from 240 ± 50 to $107 \pm 5 \text{ } \Omega \text{ cm}^2$ for QSPE-1 and QSPE-3, respectively. The less resistive interface and higher T^+ of QSPE-3 result in a correspondingly higher steady-state current [Table 3] and may result in better Li plating/stripping performance for this electrolyte.

The oxidative stability of QSPEs was analyzed by LSV and floating tests, as described in the experimental section. The use of cc-Al working electrodes allowed studying the oxidative stability of the SPEs in conditions resembling the operational cell conditions, as cc-Al is used as a current collector for the NMC-811 cathodes. A higher oxidative current and lower oxidative stability were expected due to larger electrochemical surface area and possible catalytic activity of carbon coating. Furthermore, possible

Table 3. Selected transport parameters for supported QSPEs and Li|QSPE|Li cells: ionic conductivity at room temperature, Li^+ transference number, Li/QSPE interface resistance in Li||Li cells, and steady-state current by applying a constant polarization ΔV of 10 mV

	σ (25 °C)/mS cm ⁻¹	T^+	R_{int}^+ / Ω cm ²	I_{ss} / μA
QSPE-1	1.2 ± 0.2	0.09 ± 0.01	240 ± 50	29 ± 5
QSPE-2	1.4 ± 0.3	0.12 ± 0.01	140 ± 20	47 ± 6
QSPE-3	1.2 ± 0.3	0.14 ± 0.01	107 ± 5	59 ± 2

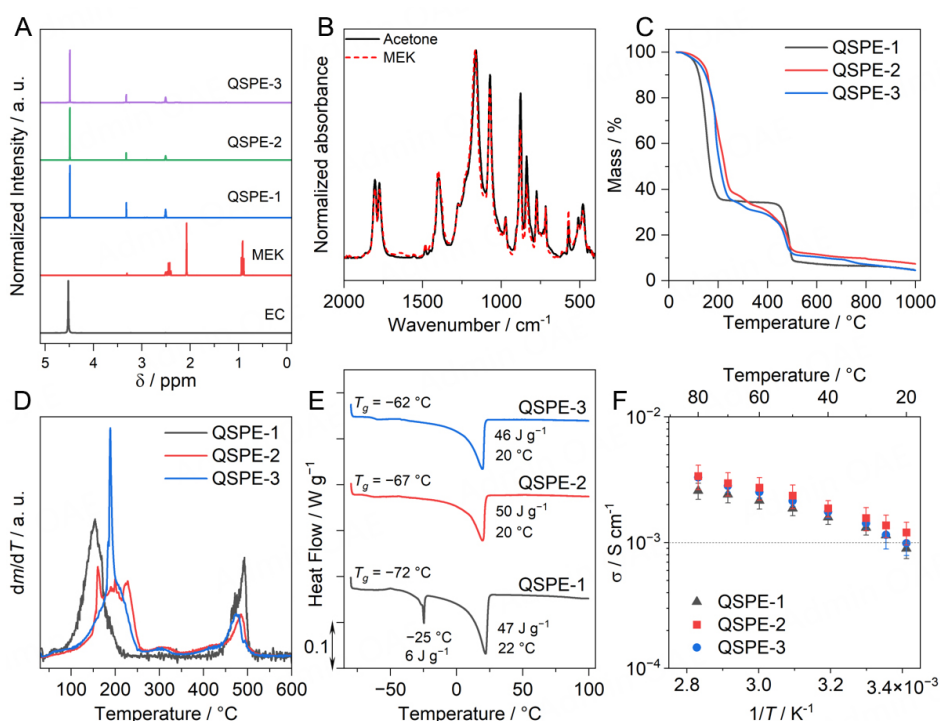


Figure 1. Chemical, thermal and transport characterization of supported QSPEs: (A) ^1H NMR spectra of the three QSPEs in DMSO, together with the ^1H NMR spectra of ethylene carbonate (EC), and methylethylketone (MEK); (B) FTIR spectra of QSPE-2, processed in acetone and MEK, between 400 and 2,000 cm^{-1} ; (C) thermogravimetric profiles, collected under Ar atmosphere, at a heating rate of 10 $^\circ\text{C min}^{-1}$, between room temperature and 1,000 $^\circ\text{C}$; (D) Derivative TGA profiles, up to 600 $^\circ\text{C}$; (E) DSC profiles, collected at a heating rate of 2 $^\circ\text{C min}^{-1}$, between -80 and 100 $^\circ\text{C}$ (cycle 2); (F) Ionic conductivity vs. temperature, between 20 and 80 $^\circ\text{C}$ (average of three cells).

corrosion phenomena involving the Al foil could contribute to the parasitic current at high voltages. The LSV profiles are shown in Figure 2. LSV was conducted at an ultra-low scan rate of 5 $\mu\text{V s}^{-1}$ to mimic the residence time in the floating current test and avoid any capacitive contribution. The oxidative stability limit for QSPE-1 is quite low, 4.2 V vs. Li/Li⁺. LSV conducted with SS working electrodes on unsupported QSPEs showed a slightly higher oxidative potential of 4.3 V vs. Li/Li⁺ [Supplementary Figure 6]. Addition of LiBOB (QSPE-2) results in an increase of the oxidative stability, with a current density of 0.5 $\mu\text{A cm}^{-2}$ at 4.4 V vs. Li/Li⁺ and a marked increase from 4.5 V vs. Li/Li⁺. A similar result was also observed in SS||Li cells, in which the electrolyte containing a mixture of LiFSI and LiBOB showed much higher stability than the electrolyte containing LiFSI only. QSPE-3 shows intermediate stability, with the current increasing slowly from 4.3 V vs. Li/Li⁺ and a steep increase from 4.4 V vs. Li/Li⁺. After the oxidation onset, the current increases much more steeply with the LiNO₃-containing QSPE-3, indicating that this salt may be deleterious for the oxidative stability of the electrolyte. LiBOB, on the other hand, is confirmed as a fundamental CEI-forming

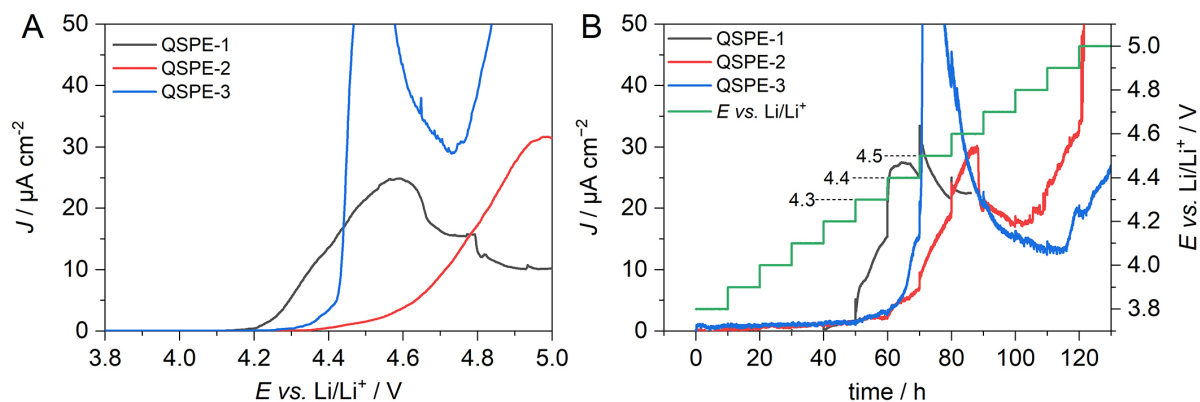


Figure 2. (A) LSV profiles of cc-Al||Li cells with different QSPEs, at 25 °C and $5 \mu\text{V s}^{-1}$; (B) floating current profiles of cc-Al||Li cells, with different QSPEs, collected at 25 °C and with step time of 10 h every 100 mV, between 3.8 and 5.0 V vs. Li/Li⁺.

additive for stabilizing the electrolyte at high voltages^[1,38]. Analogue results were obtained also in the floating current tests [Figure 2B]. QSPE-1 showed a steep current increase already at 4.3 V vs. Li/Li⁺, while QSPE-2 and QSPE-3 were stable up to at least 4.4 V vs. Li/Li⁺. Additionally, in this case, the current increase was much steeper for QSPE-3 than for QSPE-2, indicating faster oxidation or current collector corrosion for the LiNO₃-containing electrolyte.

Plating-stripping performance

The plating/stripping performance of the QSPEs was evaluated by galvanostatic cycling in Li||Li cells at room temperature, with a constant plated/stripped capacity of 2 mAh cm⁻² and current density ranging from 0.2 to 2 mA cm⁻². Constant capacity mode allows a performance comparison among electrolytes at an area capacity comparable to the one of practical full cells. The study focused on QSPE-2 and QSPE-3 due to their higher oxidative stability than QSPE-1. Initially, Li|QSPE-2|Li cells with 500 μm-thick Li electrodes were cycled to evaluate the performance of this QSPE with a large excess of Li.

The voltage vs. time profile of one of the cells cycled is shown in Figure 3A. The cell showed very low polarization even at a C-rate of 1C (2 mA cm⁻²) and excellent cyclability at C/10, with stable performance for up to 1,000 h. After 1,000 h, the polarization gradually increased, and the cell underwent a short circuit after 1,500 h cycling. The excellent Li plating/stripping performance, compared to that of unsupported QSPEs at the same capacity [Supplementary Figure 2], confirms the importance of adding a mechanical barrier to the growth of lithium dendrites. Subsequently, cells were also cycled with thin Li-Cu electrodes to assess the effect of the lithium amount. The voltage vs. time profiles of Li-Cu|QSPE-2|Li-Cu and Li-Cu|QSPE-3|Li-Cu are shown in Figure 3B and C, respectively. These cells showed higher overvoltage compared to those with thick Li electrodes, approaching 1 V at 1C. Nonetheless, cycling remained stable, and the two cells shown passed the rate test without experiencing short circuits. However, the occurrence of short circuits was observed on other replicas (results not shown), reflecting the harsh cycling conditions at high C-rates. The low reproducibility of the short circuit occurrence at high C-rates hinders the use of this parameter for the comparison of the different QSPEs. The polarization, on the contrary, is quite reproducible among different cells and is thus a convenient parameter for evaluating the plating/stripping performance. Between the two QSPEs, QSPE-3 showed lower polarization, suggesting a beneficial effect of LiNO₃. A closer examination of the voltage vs. capacity profiles shows that the higher polarization with thin Li-Cu electrodes, compared to the cells with thick Li electrodes, was caused by a voltage spike towards the end of each plating/stripping semi-cycle, which was not observed in cells with thick Li electrodes (compare Figure 3D and E). This voltage spike is attributed to Li depletion in the thin Li-Cu electrodes. On the contrary, the plateau voltage

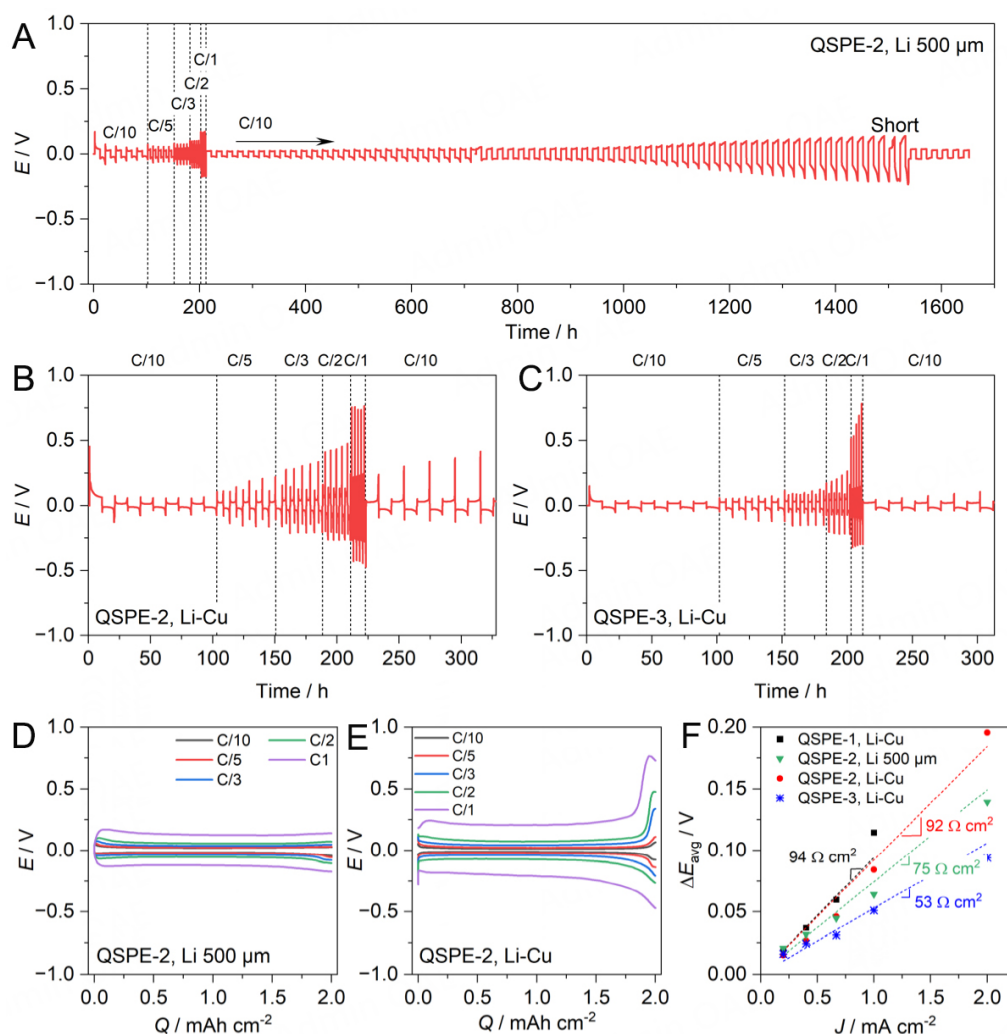


Figure 3. Plating/stripping performance of Li||Li cells with supported QSPEs, at room temperature and with plating/stripping capacity of 2 mAh cm^{-2} . (A) Galvanostatic cycling of a Li|QSPE-2|Li cell, with $500 \mu\text{m}$ -thick Li electrodes; (B) Galvanostatic cycling of a Li-Cu|QSPE-2|Li-Cu cell, with thin Li-Cu electrodes; (C) Galvanostatic cycling of a Li-Cu|QSPE-3|Li-Cu cell, with thin Li-Cu electrodes; (D) voltage vs. capacity profile at different C-rates of a Li|QSPE-2|Li cell with $500 \mu\text{m}$ -thick Li electrodes (fifth cycle at each C-rate); (E) voltage vs. capacity profile at different C-rates of a Li-Cu|QSPE-2|Li-Cu cell (fifth cycle at each C-rate); (F) average plateau voltage vs. current density, with different cell configurations. The dashed lines represent the interpolation of the experimental points, and the slope was used to estimate the internal cell resistance in steady-state conditions.

in the middle of each semi-cycle is relatively comparable in all cells. Thus, the average value of the plateau voltage was used to compare the performance of the different QSPEs. The average values of plateau voltage at different C-rates were plotted vs. the current density and interpolated [Figure 3F], and the resulting slope was used to estimate the internal cell resistance in steady-state conditions, that is, before the onset of the additional polarization due to Li depletion. The values for Li-Cu|QSPE-1|Li-Cu cells are also provided for comparison (voltage profiles are shown in Supplementary Figure 7). The internal resistance for Li|QSPE-2|Li cells is $75 \Omega \text{ cm}^{-2}$, lower than the one of Li-Cu|QSPE-2|Li-Cu cells ($92 \Omega \text{ cm}^{-2}$). The difference is possibly due to variations in internal cell pressure (despite reducing the number of spacers in cells with thick Li electrodes compared to those with Li-Cu electrodes), or it may result from differences in the wettability of the QSPEs with the two types of Li electrodes. This variation reflects the better cycling performance obtained with thick Li electrodes. Li-Cu|QSPE-1|Li-Cu cells showed a similar resistance of $94 \Omega \text{ cm}^{-2}$,

whereas Li-Cu|QSPE-3|Li-Cu cells showed the lowest internal resistance of $53 \Omega \text{ cm}^{-2}$, thus confirming the beneficial effect of LiNO_3 for the plating/stripping process.

The effect of LiNO_3 on the plating/stripping process was further examined by cycling in Cu||Li cells. The protocol described in the experimental section (Equation 3) was used to calculate the average coulombic efficiency of 50 plating/stripping cycles in Cu||Li cells with QSPE-2 and QSPE-3 as electrolytes. Again, QSPE-3 showed far better performance than QSPE-2, with an average coulombic efficiency of $99.3\% \pm 0.1\%$, compared to $95.4\% \pm 0.7\%$ of QSPE-2 [Supplementary Figure 8 and Supplementary Figure 9]. The results further confirm the positive effect of LiNO_3 on the Li plating/stripping process and suggest that the LiNO_3 salt additive protects the electrolyte from decomposition at the Li interface. To confirm this hypothesis, XPS analysis was performed on Cu electrodes recovered from Cu||Li cells, cycled either with QSPE-2 or QSPE-3. The cells were cycled with a similar profile to the previous cells but were left in the plated state; that is, the last stripping semi-cycle was not performed. For comparison, XPS spectra were also collected on Cu electrodes cycled only for three cycles at a capacity of 2 mAh cm^{-2} and at a current density of 0.1 mA cm^{-2} (fully stripped Cu electrodes), and on Cu electrodes cycled for two and a half cycles in the same conditions (fully plated Cu electrodes). The three cycling profiles are shown in Supplementary Figure 10. The aim was to study the evolution of the SEI throughout the plating/stripping process and its long cycling stability. Although the SEI formed on Cu might differ from the one formed on $\text{Li}^{[59]}$, this comparative study was useful to assess the effect of LiNO_3 on the electrolyte stability at the anode interface. The XPS spectra collected on the cycled Cu electrodes are shown in Figure 4, whereas those of stripped and plated Cu electrodes are shown in Supplementary Figure 11 and Supplementary Figure 12, respectively.

The most significant difference between the electrodes cycled with QSPE-2 and QSPE-3 lies in the relative concentration of FSI⁻ anion decomposition products compared to the FSI⁻ residuals. As seen in Figure 4, FSI⁻ residuals are more intense in the Cu electrode cycled with QSPE-3, whereas the signals of the FSI⁻ decomposition products (e.g., LiF in the F 1s spectrum, SO_x signal in the S 2p spectrum) are much weaker. Therefore, the addition of LiNO_3 limits the FSI⁻ reduction by Li. In addition, the fitting of the B 1s spectrum of the electrode cycled with QSPE-2 evidences the lack of BOB⁻ anion residuals, while other boron oxides are present, indicating that in the vicinity of the Cu electrode, this anion is completely decomposed during plating. This finding agrees with the reported reduction potential of BOB⁻ at $\sim 1.8 \text{ V vs. Li/Li}^+$. On the contrary, in the case of QSPE-3, a weak signal of BOB⁻ is still present, indicating that LiNO_3 partially protects this anion from decomposition. The lower reduction of FSI⁻ and BOB⁻ anions when LiNO_3 is present in the electrolyte seems to indicate a reduced electrolyte consumption likely by forming a more effective SEI rich in LiNO_3 decomposition products. Interestingly, no signal from Li_3N was clearly observed, suggesting that this SEI component, if present, might be buried more deeply in the SEI to be visible by XPS.

Similar results were also obtained with Cu electrodes analyzed after three full Li plating/stripping cycles (stripped Cu electrodes, Supplementary Figure 11) and after two and a half cycles (plated Cu electrodes, Supplementary Figure 12), except that, in the latter case, the BOB⁻ signal was observed as well when QSPE-2 was employed, although in minor concentration with respect to the case of QSPE-3. The relative concentration of the different components is reported in Supplementary Figure 13, also showing similar SEI composition in the different cycling stages, indicating quite stable chemistry throughout cycling. Larger differences were observed in the C 1s spectrum, between the electrodes cycled with QSPE-2 and QSPE-3, which may be caused by the presence of adventitious carbon and the rest of the electrolyte polymer matrix. Nevertheless, the systematically higher content of carbon bonds in the electrodes cycled with QSPE-2 vs. those cycled with QSPE-3, especially in form of hydrocarbon, C-O and COO, may denote a more organic SEI due to higher solvent decomposition. Altogether, the XPS analysis evidenced the effectiveness of LiNO_3

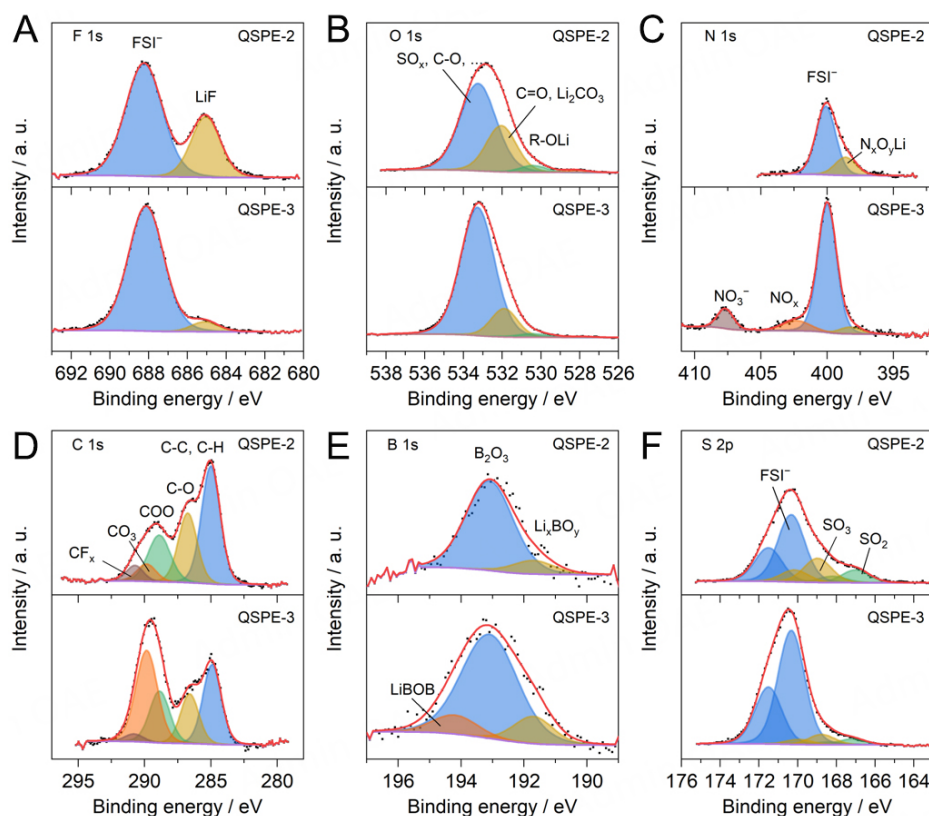


Figure 4. X-ray photoelectron spectra of Cu electrodes recovered from Cu||Li cells, cycled either with QSPE-2 (upper panels) or QSPE-3 (lower panels) as electrolyte. Cycling was performed at room temperature, with two and a half cycles at 2 mA h cm^{-2} and 0.1 mA cm^{-2} , followed by 50 cycles at 0.2 mA h cm^{-2} and 0.1 mA cm^{-2} . (A) F 1s, (B) O 1s, (C) N 1s, (D) C 1s, (E) B 1s and (F) S 2p core levels with corresponding fittings based on internal references as well as ^[38,60,61] and refs therein.

in protecting the electrolyte from intense reduction by metallic lithium, preventing the other anions and the solvent from strong decomposition, which has a beneficial effect on the plating/stripping coulombic efficiency.

Full cell performance

The full cell performance of QSPE-2 and QSPE-3 was first evaluated in NMC-811||Li-Cu cells, in coin cell configuration, with NMC-811 synthesized by spray drying and with cathode active material loading of $\sim 13 \text{ mg cm}^{-2}$. The cells were cycled at room temperature, with C-rates ranging from C/20 to 1C, and then at a constant C-rate of C/10. The specific discharge capacity of two cells with QSPE-2 and QSPE-3, during the first 150 cycles, is depicted in [Figure 5A](#), whereas the corresponding coulombic efficiency and capacity retention during the long cycling at C/10 are shown in [Figure 5B](#) and [C](#), respectively. The complete discharge capacity profile of three cells with QSPE-3, up to 220 cycles, is shown in [Supplementary Figure 14](#). The cell with QSPE-3 delivered slightly higher specific capacity during the initial C-rate test, with initial specific discharge capacity of 165 mA h g^{-1} at C/20 and $\sim 60 \text{ mA h g}^{-1}$ at C/1. During the rate test, the capacity decay is faster at low C-rates, which might be due to the longer residence time at high voltages and thus to a more severe electrolyte degradation. In the subsequent long cycling at C/10, the capacity fading rate was initially lower for the cell with QSPE-2, so that after 80 cycles, the capacity was approximately equal for both cells. In this initial range, the capacity retention was similar or slightly higher for QSPE-2 than for QSPE-3 (region I in [Figure 5C](#)). Nonetheless, after cycle 80, the cell with QSPE-2 started to lose capacity more rapidly and underwent sudden failure after approximately 130 cycles. On the contrary, the cell with QSPE-3

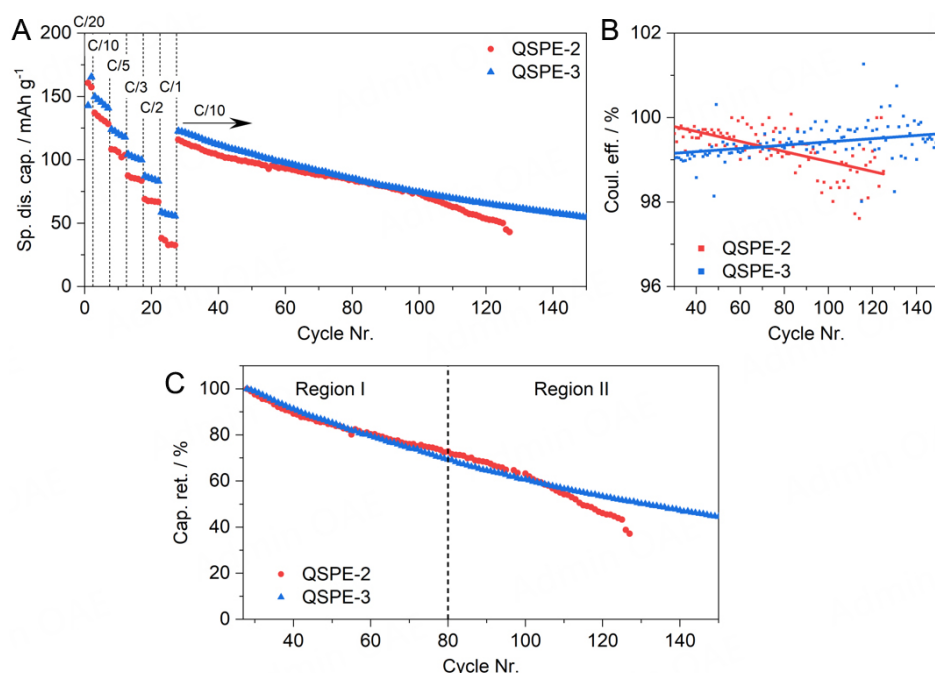


Figure 5. Galvanostatic cycling of NMC-811||Li-Cu coin cells with QSPE-2 and QSPE-3, performed at room temperature, in the voltage range between 3.0 and 4.3 V, and with cathode active material loading of $\sim 13 \text{ mg cm}^{-2}$. (A) Specific discharge capacity during the first 150 cycles; (B) coulombic efficiency during the long cycling at C/10; (C) Capacity retention during the long cycling at C/10, normalized on the first cycle at C/10 after C-rate test.

cycled for over 200 cycles without showing sudden failure, despite with a continuous capacity fade [Supplementary Figure 14]. The trends in the capacity fade correlate with some slight differences observed in the coulombic efficiency during long cycling. Initially, the cell with QSPE-2 has higher coulombic efficiency, concordant with the lower capacity fade rate. However, during the subsequent cycling, the coulombic efficiency decreased continuously for QSPE-2, while increasing for cells with QSPE-3. The coulombic efficiency dropping below 99% for QSPE-2 coincides with the sudden capacity drop observed in this cell. This is probably caused by the depletion of the cyclable Li in the anode^[62], exacerbated by the low amount of Li reservoir on the anode ($\sim 20 \mu\text{m}$). This effect was not observed with QSPE-3 for over 200 cycles, which is attributed to the higher coulombic efficiency for the lithium plating/stripping process in presence of LiNO_3 . To summarize, the aging behavior of the analyzed cells is characterized by two distinct regions. In the first region, the cells experience linear capacity fade, slightly more accelerated for cells with QSPE-3 than cells with QSPE-2. In the second region, which is dominated by anode depletion, the cells undergo sudden capacity fade. The onset of this second aging regime is delayed in cells with QSPE-3 as an electrolyte.

EIS study in two- and three-electrode cell configurations

To understand the origin of the different behavior with the two electrolytes, two other cells were cycled at a constant C-rate of C/10 (after a formation cycle at C/20). In addition, EIS spectra were collected at the EoD, every 5 cycles, in the frequency range between 10 kHz and 10 mHz. The specific discharge capacity and coulombic efficiency of the two cells are represented in Figure 6A. The discharge capacity in the initial cycles was similar, namely 164 and 161 mAh g^{-1} at C/20 and 142 and 138 mAh g^{-1} at C/10 for QSPE-2 and QSPE-3, respectively. In this experiment, no sudden failure was observed, presumably because cycling was stopped before this mode of failure occurred. However, as in the previous experiment, the two cells showed a constant capacity decrease, with slightly better cyclability for the cell with QSPE-2. The capacity fade rate

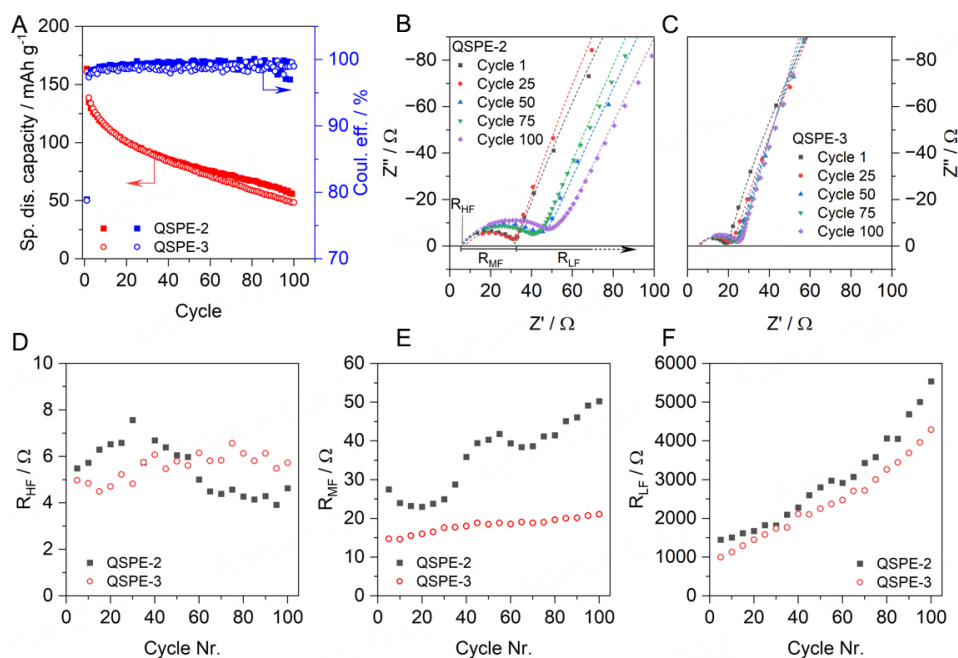


Figure 6. Galvanostatic cycling of two NMC-811||Li-Cu cells with QSPE-2 and QSPE-3 as electrolyte, coupled with EIS analysis. Galvanostatic cycling was performed at room temperature, in the voltage range between 3.0 and 4.3 V, and at constant C-rate of C/10 (with one initial cycle at C/20). The cathode active material loading was $\sim 13 \text{ mg cm}^{-2}$. EIS spectra were collected at the end of discharge, every 5 cycles. (A) Specific discharge capacity (left axis) and coulombic efficiency (right axis); (B) selected EIS spectra of the cell with QSPE-2. Dots represent experimental curves and dashed lines of the fitting curves; (C) selected EIS spectra with QSPE-3. Dots represent the experimental curves and dashed lines of the fitting curves; (D-F) evolution of the (D) high-frequency, (E) middle-frequency, and (F) low-frequency resistance components upon cycling.

was similar in the two cases [Supplementary Figure 15], but the final capacity retention at cycle 100, with respect to the first cycle at C/10, was slightly higher for QSPE-2, namely 42% vs. 35% for QSPE-2 and QSPE-3, respectively. Concordantly, the coulombic efficiency was higher for QSPE-2, with average values (excluding the formation cycle) of 99.2% and 98.7%, respectively. The EIS spectra upon cycling were analyzed to shed light on the origin of the capacity fade. The full EIS spectra are shown in Supplementary Figure 16, whereas Figure 6B and C shows the zoom on high-frequency region of the spectra. The spectra are characterized by a small high-frequency semicircle, in the range from 10 kHz-100 Hz, followed by a large semicircle at lower frequencies. Thus, the spectra were fitted with a ladder equivalent circuit model comprising three resistances, labeled high-frequency resistance (R_{HF}), middle-frequency resistance (R_{MF}), and low-frequency resistance (R_{LF}), and two constant phase elements [Supplementary Figure 17]. As customary, the R_{HF} was attributed to the sum of the cell ohmic resistances, among which the main contribution is probably the bulk electrolyte resistance, whereas the middle-frequency semicircle (R_{MF}) was assigned to the sum of the different planar interface resistances, such as the cathode/QSPE and anode/QSPE interface resistances, and the cathode-current collector contact resistance. Since the area of these interfaces is similar, corresponding to the geometrical area of the cell, their EIS contributions are expected to be highly overlapped and appear in the middle-high frequency region^[63,64]. Finally, the lowest resistive contribution (R_{LF}) was assigned to the cathode charge transfer resistance^[65,66]. R_{LF} is several orders of magnitude larger than the other two resistances, which agrees with the expected dependence of the charge transfer resistance on the state of charge, particularly the expected increase towards the EoC/EoD^[67].

The evolution of the three resistances upon cycling is shown in Figure 6D-F. R_{HF} was approximately constant upon cycling and similar for the two electrolytes, concordant with the similar ionic conductivity of the two QSPEs. R_{MF} was initially 28 and 15 Ω for QSPE-2 and QSPE-3, respectively. R_{MF} increased steadily upon cycling, with a more pronounced rise observed for QSPE-2. This trend agrees with the less resistive and more stable anode interface obtained using LiNO_3 , as observed in $\text{Li}||\text{Li}$ cells [Supplementary Figure 5], and suggests that R_{MF} is strongly influenced by the resistance of the anode/QSPE interface. Although XPS analysis indicated stable SEI chemistry for QSPE-2, the SEI thickness likely increases during cycling due to the higher propensity of QSPE-2 for reduction by the lithium anode. Finally, R_{LF} increased steadily upon cycling, similarly for the two QSPEs, indicating progressive deterioration on the cathode side. This might be due to various processes, such as progressive oxidation of the electrolyte, degradation of the active material (e.g., cracking), or loss of contact between the electrolyte and the cathode active material particles upon repeated lithiation/delithiation cycles. Among the three resistive components, the increase of R_{LF} was the most evident, from *ca.* 1,000 Ω to *ca.* 5,000 Ω at the end of cycling, thus suggesting that the progressive capacity decay may be due to the increase of the cathode charge transfer resistance.

In conclusion, the EIS analysis in two-electrode cell configuration suggests that the progressive capacity fade is mainly associated with the degradation of the cathode interface. In this regard, LiNO_3 has, apparently, a negligible effect. Besides, a progressive increase of R_{MF} , associated with a progressive deterioration of the anode interface, was observed in the cell with QSPE-2, while this effect was less obvious in the cell with QSPE-3. This agrees with the previous results from $\text{Cu}||\text{Li}$ cells characterizations, indicating a higher propensity of QSPE-2 to reductive decomposition on the lithium anode.

The effect of LiNO_3 on the cyclability of $\text{NMC-811}||\text{Li}$ cells was further studied by cycling three-electrode cells at $C/20$ for 30 cycles, while collecting EIS spectra both at the EoD and at the EoC. The two cycled cells, with QSPE-2 and QSPE-3 as electrolytes, showed decreasing capacity, as observed in the previous experiments, with slightly faster fading for the cell with QSPE-3 [Figure 7A]. The coulombic efficiency was initially higher for the cell with QSPE-2, although it became approximately equal after *ca.* 15 cycles. So far, this confirmed the conclusion from previous experiments that the addition of LiNO_3 initially worsens the cyclability, although during long cycling, it has a positive effect due to reduced consumption of Li at the anode. We then focused our attention on the positive electrode, trying to clarify whether the addition of LiNO_3 affects cathode aging. Figure 7B shows the open circuit potential of the positive electrode ($E_{+,OCP}$), against the lithium metal reference electrode upon cycling time. While the potential at the EoD remained approximately constant, it decreased progressively at the EoC, indicating a decreased ability to extract Li^+ from the cathode active material upon cycling. This could be attributed to a partial disconnection of the cathode active material particles upon cycling and is obviously related to the linear capacity decay of the cycled $\text{NMC-811}||\text{Li}$ cells. Between the two cells, the decrease of the $E_{+,OCP}$ is faster with QSPE-3, in agreement with the faster capacity decay, thus suggesting that the cathode aging is accelerated in presence of LiNO_3 . As mentioned above, EIS spectra were collected both at the EoC and at the EOD. Selected EIS spectra of the positive electrodes are shown in Supplementary Figure 18 (QSPE-2) and Supplementary Figure 19 (QSPE-3). The spectra show two semicircles in the high/middle frequency range, clearly separated in the case of QSPE-2 and more overlapped in the case of QSPE-3, followed a large semicircle at low frequencies. The spectra can be modeled through a ladder circuit encompassing four resistances and three constant phase elements [Supplementary Figure 20]. The high-frequency series resistance (R_{HF}) is related to the electrolyte ionic resistance, whereas the R_{MF} ($R_{MF,1}$ and $R_{MF,2}$) is tentatively attributed to the planar cathodic interface resistances, namely the interface resistance between the cathode and the QSPE, and to the contact resistance between the cathode and the current collector. Indeed, planar interfaces should give rise to impedance features in the middle-/high-frequency range^[63,68], and in the system

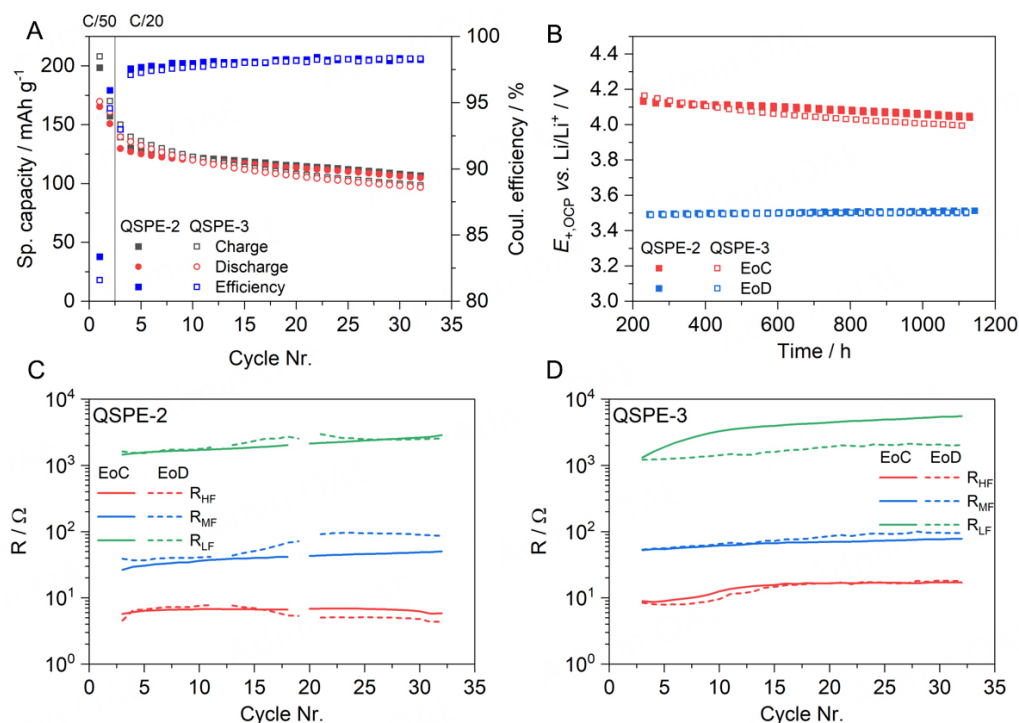


Figure 7. EIS analysis of three-electrode NMC-811||Li-Cu cells with QSPE-2 and QSPE-3 as electrolytes. Cells were cycled between 3.0 and 4.3 V, at C/50 (2 cycles) and C/20 (30 cycles). EIS spectra were collected during cycling at C/20, at the end of charge (EoC) and at the end of discharge (EoD), after one hour of resting. (A) Specific capacity (left axis) and coulombic efficiency (right axis); (B) open circuit potential of the positive electrode ($E_{+,OCp}$) vs. Li/Li⁺, at the EoC and EoD, upon cycling time (each point corresponds to one cycle at C/20); (C) evolution of the main resistances of the positive electrode impedance spectra, at the EoC and EoD, with QSPE-2 as electrolyte; (D) evolution of the main resistances contributing to the positive electrode impedance spectra, at the EoC and EoD, with QSPE-3 as electrolyte.

under consideration, once the anode contribution is removed, the only planar interfaces remaining are the QSPE/cathode solid interface and the interface between the current collector and the cathode layer. Finally, as mentioned above, the low-frequency component (R_{LF}) is attributed to the cathode charge transfer resistance. Each resistance is associated with a parallel capacitance that can be calculated from the CPEs, as described by Brug *et al.* The product of the resistances by their associated capacitances gives the characteristic time constants for the related polarization phenomena^[69]. The time constants for the middle- and low-frequency polarizations are shown in [Supplementary Figure 21](#). The middle-frequency polarizations have time constants comprised between 10^{-6} and 10^{-4} s ($\tau_{MF,1}$) and between 10^{-3} and 10^{-2} s ($\tau_{MF,2}$). The low-frequency polarization has a very high characteristic time constant $\tau_{LF} > 10$ s. The time constants are approximately constant upon cycling. That is, if a resistance increases upon cycling, the associated capacitance decreases. $\tau_{MF,2}$ and τ_{LF} have similar values in QSPE-2 and QSPE-3-containing cells. However, $\tau_{MF,1}$ is an order of magnitude higher for QSPE-3, with respect to QSPE-2, which explains the higher degree of overlap between the two middle-frequency semicircles with the former electrolyte.

The evolution of the resistance components upon cycling is shown in [Figure 7C](#) (QSPE-2) and [Figure 7D](#) (QSPE-3). The overlapping between the middle-frequency impedance components in QSPE-3 spectra results in a high degree of uncertainty on the related resistances. For a better comparison between the two electrolytes, the sum of the R_{MF} was considered in the analysis. The R_{HF} is insensitive to the state of charge and was stable upon cycling, indicating that the bulk properties of the electrolyte are not affected during these few cycles. R_{MF} increases moderately upon cycling for both electrolytes. The value is initially higher for

QSPE-3 (27 vs. 53 Ω at the EoC), but the increase is more pronounced for QSPE-2, namely 90% vs. 47%. A slight divergence between EoC and EoD is observed, especially in the case of QSPE-2. The increase upon cycling suggests a progressive degradation of the cathode/QSPE interface, or a progressive loss of contact between the cathode-coated layer and the current collector. The higher resistance of the middle-frequency component and the higher value of the time constant $\tau_{MF,1}$, with QSPE-3, suggest a more sluggish charge transfer across the cathode/QSPE interface. However, the most striking differences are observed in the R_{LF} . In the case of QSPE-2, R_{LF} increases from $\sim 1,500$ to $\sim 2,500$ Ω after 30 cycles, with similar values at the EoC and EoD. As for the two-electrode cells, the high values of cathode charge transfer resistance are caused by the blocking behavior of the cathode in the fully lithiated/delithiated states. For QSPE-3, however, the increase at the EoC is much more pronounced. R_{LF} increases from 1,200 to 2,000 Ω at the EoD, and from a similar initial value to 5,500 Ω at the EoC. This increase suggests a faster degradation of the cathode interface at high voltages, possibly involving oxidation of the catholyte, and may explain the faster capacity decay with the LiNO_3 -containing QSPE-3. The EIS analysis in a three-electrode cell configuration confirms the results from LSV and floating current experiments, showing faster electrolyte oxidation for QSPE-3 with respect to QSPE-2. It is interesting that this effect was not observed in the two-electrode cell, as in that case, the EIS spectra were collected at the EoD. The study remarks the importance of collecting EIS spectra at the EoC during cycling, rather than at the EoD, as degradation effects due to high voltage may be visible only in the charged state.

To sum up, the addition of LiNO_3 improved the coulombic efficiency for the lithium plating/stripping process, delaying sudden cell failure due to lithium depletion at the anode. However, the primary cause for capacity fade in this type of cell appears to be related to the degradation of the positive electrode or the related electrolyte interface. In this regard, the addition of LiNO_3 did not show any significant benefit. On the contrary, cells containing LiNO_3 showed slightly lower coulombic efficiency and higher capacity fade rate, possibly due to accelerated electrolyte oxidation at high voltages. In addition, EIS analysis in a three-electrode cell configuration showed that this accelerated capacity fade is related to a steeper increase of the cathode charge transfer resistance at the EoC, and thus to a faster degradation of the cathode active material in the delithiated state, or to a faster oxidation of the electrolyte/catholyte at high voltages. This effect, which is further confirmed by the previous results from LSV and floating experiments, might be due to several factors, such as crossover of the LiNO_3 decomposition products from the anode to the cathode, a catalytic activity towards electrolyte oxidation, or LiNO_3 interference with the formation of the LiBOB-borne CEI.

Pouch cell performance

To complete the study, a monolayer pouch cell with QSPE-2 as an electrolyte was assembled and cycled, first at different C-rates, and then at a constant C-rate of C/10. Figure 8 shows the specific capacity and coulombic efficiency of this cell. The initial specific capacity of this cell (at C/20) was close to 200 mAh g^{-1} , close to the theoretical specific capacity of NMC-811. The higher capacity obtained with this cell, compared to the previous results in coin cells, is attributed to the use of commercial, optimized NMC-811, while non-optimized research-grade NMC-811 was used for the study of coin cells. The cell showed also excellent C-rate capability, with a specific capacity of 150 mAh g^{-1} at 1C, despite having a cathode with high area capacity of 2.5 mAh cm^{-2} . The cyclability was also good, with a capacity retention of 80% reached after ca. 90 cycles. No sudden failure was observed over 160 cycles, possibly thanks to a higher and more homogeneous pressure distribution in the pouch cell format. The average coulombic efficiency, during the long cycling at C/10, was over 99.5%.

Altogether, the results confirm the suitability of this QSPE for application in high-voltage quasi-solid-state lithium metal batteries, although its cyclability must be further improved to meet the requirements for practical use. The limited cyclability arises from the degradation of the electrolyte/catholyte at high voltages,

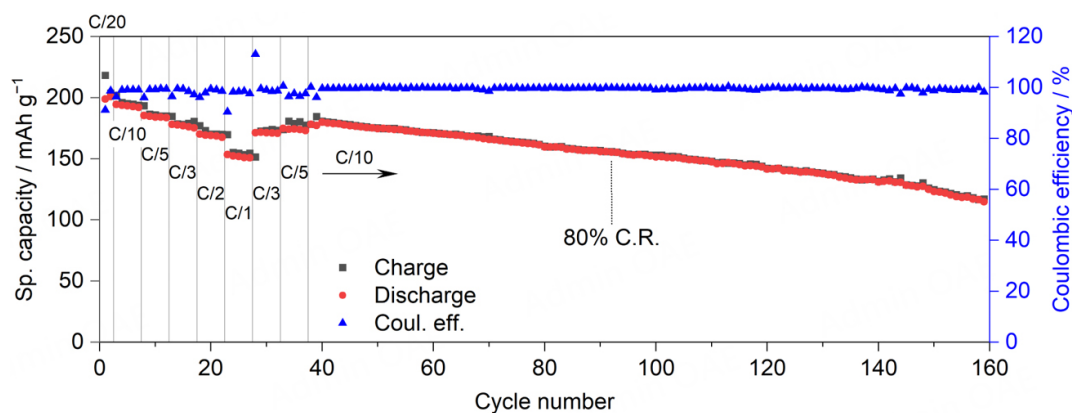


Figure 8. Full cell performance of a NMC-811||Li-Cu monolayer pouch cell with QSPE-2 as electrolyte. Galvanostatic cycling was performed at room temperature, between 3.0 and 4.3 V (see Table 2 for detailed cycling protocol). The nominal area capacity for this cell was 2.5 mAh cm^{-2} .

the chemical reactivity of delithiated NMC-811, and lithium depletion at the anode during cycling. These issues are further exacerbated when cycling at high area capacities, which are necessary for achieving high energy densities^[70]. Tackling these challenges will require comprehensive optimization of all cell components and their interfaces^[71]. For instance, electrolyte degradation at the cathode interface could be mitigated by applying coatings to the cathode active material particles^[72-74] or further refining the electrolyte formulation. Improving cyclability will also necessitate enhancing the plating-stripping coulombic efficiency. Lithium reactivity at the anode could be reduced by applying a passivation layer on its surface^[75-77]. Additionally, the use of SEI-forming additives, such as LiNO_3 , has proven highly effective, as demonstrated in our work.

CONCLUSIONS

In this study, QSPEs based on PVdF-HFP and EC with various salt mixtures (LiFSI in QSPE-1, LiFSI/LiBOB in QSPE-2, and LiFSI/LiBOB/ LiNO_3 in QSPE-3) were developed and characterized. The QSPEs exhibited ionic conductivities near 1 mS cm^{-1} at room temperature and oxidative stability increasing in the order QSPE-1 < QSPE-3 < QSPE-2. Adding LiBOB improved oxidative stability, while LiNO_3 had a detrimental effect, compared to the LiFSI/LiBOB binary salt mixture.

QSPEs supported on micro-porous polyolefin separators showed enhanced resistance against lithium dendrite growth, enabling 2 mAh cm^{-2} plating/stripping in Li||Li cells. Supporting QSPEs on microporous separators was demonstrated to be a promising strategy for cycling lithium metal batteries at high area capacities. QSPE-3, containing LiNO_3 , demonstrated superior performance in galvanostatic cycling and coulombic efficiency in Cu||Li cells. XPS analysis revealed that LiNO_3 reduced salt decomposition, enhancing plating/stripping efficiency.

In NMC-811||Li-Cu cells with $\sim 13 \text{ mg cm}^{-2}$ cathode loading and $20 \text{ }\mu\text{m}$ lithium anode, QSPE-2 failed after 120 cycles due to lithium depletion. QSPE-3 avoided sudden failure but showed accelerated capacity fade due to cathode interface degradation, attributed to LiNO_3 -induced electrolyte oxidation. While LiNO_3 benefits the anode/electrolyte interface, it negatively affects the electrolyte oxidative stability.

QSPE-2 was further tested in an $\sim 80 \text{ mAh}$ NMC-811||Li-Cu pouch cell with practical configuration, namely with 2.5 mAh cm^{-2} area capacity and $20 \text{ }\mu\text{m}$ -thick lithium metal anode. The pouch cell achieved good

cycling performance, with 200 mAh g⁻¹ at C/20, 150 mAh g⁻¹ at 1C, and 80% capacity retention after 100 cycles at C/10.

DECLARATIONS

Acknowledgments

The authors would like to express their gratitude to the European Commission for supporting the work conducted under the EU Horizon Europe project SPINMATE (Grant Agreement 101069712). They also wish to thank all the other partners of the SPINMATE consortium, including Avesta Battery & Energy Engineering (ABEE), the Fraunhofer Institute for Silicate Research (Fraunhofer ISC), COMAU SPA, the Technical University of Braunschweig, Toyota Motor Europe NV, CEA, IREC, INEGI, and INOVA+, for their invaluable contributions to this research. In particular, the authors acknowledge ABEE for providing Cu-coated lithium metal anodes (Li-Cu), Marc Nel-lo Pascual (IREC) for assistance with the development of the spray-dried NMC-811 cathode active material, Miren de Lasén (CIC energiGUNE) for support in the XPS experiments, and Jiessei Braccini (CIDETEC) for preparing positive electrodes and assembling the single-layer pouch cells.

Authors' contributions

Conceptualization, investigation, writing - original draft, writing - review & editing: Boaretto, N.

Investigation: Cobos, M.; Fernandez de Añastro, A.; Diez Viera, M.; Al Sammarraie Shakir, M.; Lindberg, S.; Cid, R.

Investigation, resources: Jøsang, L. O.

Conceptualization, investigation: Garcia-Calvo, O.

Conceptualization, resources: Godillot, G.

Conceptualization, supervision: Kvasha, A.

Supervision: Martínez-Ibañez, M.

All authors revised the manuscript.

Availability of data and materials

Additional data is available from the corresponding author upon reasonable request.

Financial support and sponsorship

This study was funded by the European Commission through the EU Horizon Europe project SPINMATE (Grant Agreement 101069712).

Conflicts of interest

Godillot, G. is employed by Arkema France, a company that develops, manufactures, and commercializes specialty materials, including PVDF and LiFSI. Other authors declared that there are no conflicts of interest.

Ethical approval and consent to participate

Not applicable.

Consent for publication

Not applicable.

Copyright

© The Author(s) 2025.

REFERENCES

1. Choudhury, S.; Tu, Z.; Nijamudheen, A.; et al. Stabilizing polymer electrolytes in high-voltage lithium batteries. *Nat. Commun.* **2019**, *10*, 3091. DOI PubMed PMC
2. Cui, S.; Wu, X.; Yang, Y.; et al. Heterostructured gel polymer electrolyte enabling long-cycle quasi-solid-state lithium metal batteries. *ACS. Energy. Lett.* **2022**, *7*, 42-52. DOI
3. Wu, F.; Chen, Z.; Fang, S.; Zuo, W.; Kim, G.; Passerini, S. The role of ionic liquids in resolving the interfacial chemistry for (quasi-) solid-state batteries. *Energy. Storage. Mater.* **2023**, *63*, 103062. DOI
4. Li, W.; Li, H.; Liu, J.; et al. Systematic safety evaluation of quasi-solid-state lithium batteries: a case study. *Energy. Environ. Sci.* **2023**, *16*, 5444-53. DOI
5. Wang, Z.; Wang, Y.; Shen, L.; et al. Towards durable practical lithium-metal batteries: advancing the feasibility of poly-DOL-based quasi-solid-state electrolytes via a novel nitrate-based additive. *Energy. Environ. Sci.* **2023**, *16*, 4084-92. DOI
6. Pan, J.; Zhao, P.; Yao, H.; Hu, L.; Fan, H. J. Inert filler selection strategies in Li-ion gel polymer electrolytes. *ACS. Appl. Mater. Interfaces.* **2024**, *16*, 48706-12. DOI
7. Yao, M.; Ruan, Q.; Yu, T.; Zhang, H.; Zhang, S. Solid polymer electrolyte with in-situ generated fast Li⁺ conducting network enable high voltage and dendrite-free lithium metal battery. *Energy. Storage. Mater.* **2022**, *44*, 93-103. DOI
8. Zhang, T.; Li, J.; Li, X.; et al. A silica-reinforced composite electrolyte with greatly enhanced interfacial lithium-ion transfer kinetics for high-performance lithium metal batteries. *Adv. Mater.* **2022**, *34*, e2205575. DOI
9. Li, L.; Wang, J.; Zhang, L.; Duan, H.; Deng, Y.; Chen, G. Rational design of a heterogeneous double-layered composite solid electrolyte via synergistic strategies of asymmetric polymer matrices and functional additives to enable 4.5 V all-solid-state lithium batteries with superior performance. *Energy. Storage. Mater.* **2022**, *45*, 1062-73. DOI
10. Qiu, G.; Shi, Y.; Huang, B. A highly ionic conductive succinonitrile-based composite solid electrolyte for lithium metal batteries. *Nano. Res.* **2022**, *15*, 5153-60. DOI
11. Wang, Q.; Su, Y.; Zhu, W.; et al. Achieving stable interface for lithium metal batteries using fluoroethylene carbonate-modified garnet-type Li_{6.4}La₃Zr_{1.4}Ta_{0.6}O₁₂ composite electrolyte. *Electrochim. Acta.* **2023**, *446*, 142063. DOI
12. Shen, C.; Feng, W.; Yu, Y.; et al. In situ polymerization inhibiting electron localization in hybrid electrolyte for room-temperature solid-state lithium metal batteries. *Adv. Energy. Mater.* **2024**, *14*, 2304511. DOI
13. Boaretto, N.; Meabe, L.; Lindberg, S.; et al. Hybrid ceramic polymer electrolytes enabling long cycling in practical 1 Ah-class high-voltage solid-state batteries with Li metal anode. *Adv. Funct. Mater.* **2024**, *34*, 2404564. DOI
14. Boaretto, N.; Meabe, L.; Martinez-ibañez, M.; Armand, M.; Zhang, H. Review-polymer electrolytes for rechargeable batteries: from nanocomposite to nanohybrid. *J. Electrochem. Soc.* **2020**, *167*, 070524. DOI
15. Marchiori, C. F. N.; Carvalho, R. P.; Ebadi, M.; Brandell, D.; Araujo, C. M. Understanding the electrochemical stability window of polymer electrolytes in solid-state batteries from atomic-scale modeling: the role of Li-ion salts. *Chem. Mater.* **2020**, *32*, 7237-46. DOI
16. Chen, L.; Venkatram, S.; Kim, C.; Batra, R.; Chandrasekaran, A.; Ramprasad, R. Electrochemical stability window of polymeric electrolytes. *Chem. Mater.* **2019**, *31*, 4598-604. DOI
17. Bao, D.; Tao, Y.; Zhong, Y.; et al. High-performance dual-salt plastic crystal electrolyte enabled by succinonitrile-regulated porous polymer host. *Adv. Funct. Mater.* **2023**, *33*, 2213211. DOI
18. Barbosa, J. C.; Pinto, R. S.; Correia, D. M.; et al. Effect of fluorinated polymer matrix type in the performance of solid polymer electrolytes based on ionic liquids for solid-state lithium-ion batteries. *Chem. Eng. J.* **2023**, *478*, 147388. DOI
19. Agnihotri, T.; Ahmed, S. A.; Tamilarasan, E. B.; et al. Anion-trapping composite gel electrolyte for safer and more stable anode-free lithium-metal batteries. *Chem. Eng. J.* **2024**, *484*, 149608. DOI
20. Deshmukh, S. P.; Das, R.; Kundu, D. Unraveling the underlying structural & transport mechanism of lithium-ion within Lithium bis(trifluoromethanesulfonyl)imide subjected to organic & inorganic matrix based Eutectogel. *J. Power. Sources.* **2024**, *600*, 234270. DOI
21. Duan, H.; You, Y.; Wang, G.; et al. Lithium-ion charged polymer channels flattening lithium metal anode. *Nanomicro. Lett.* **2024**, *16*, 78. DOI
22. Gai, Q.; Zhao, T.; Ma, J.; Wang, C.; Gao, H.; Li, L. An in-situ bicomponent polymeric matrix solid electrolyte for solid-state Lithium metal batteries with extended cycling-life. *J. Energy. Storage.* **2024**, *80*, 110150. DOI
23. Lin, Y.; Wu, L.; Zhan, Y.; et al. Self-assembly formation of solid-electrolyte interphase in gel polymer electrolytes for high performance lithium metal batteries. *Energy. Storage. Mater.* **2023**, *61*, 102868. DOI
24. Lv, Q.; Jing, Y.; Wang, B.; et al. Multilayer asymmetric solid polymer electrolyte with modified interface for high-voltage solid-state Li metal batteries. *Energy. Storage. Mater.* **2024**, *65*, 103122. DOI
25. Li, Z.; Zhang, S.; Jiang, Z.; Cai, D.; Gu, C.; Tu, J. Deep eutectic solvent-immobilized PVDF-HFP eutectogel as solid electrolyte for safe lithium metal battery. *Mater. Chem. Phys.* **2021**, *267*, 124701. DOI
26. Zhang, J.; Sun, B.; Huang, X.; Chen, S.; Wang, G. Honeycomb-like porous gel polymer electrolyte membrane for lithium ion batteries with enhanced safety. *Sci. Rep.* **2014**, *4*, 6007. DOI PubMed PMC
27. Bai, M.; Tang, X.; Zhang, M.; et al. An in-situ polymerization strategy for gel polymer electrolyte Si||Ni-rich lithium-ion batteries. *Nat. Commun.* **2024**, *15*, 5375. DOI
28. Jiang, X.; Liu, F.; Bai, M.; et al. Breaking solvation dominance of phosphate via dipole-dipole chemistry in gel polymer electrolyte.

- ACS. Energy. Lett.* **2024**, *9*, 3369-79. DOI
29. Li, X.; Li, Z.; Zhang, W.; et al. Flame-retardant in-situ formed gel polymer electrolyte with different valance states of phosphorus structures for high-performance and fire-safety lithium-ion batteries. *Chem. Eng. J.* **2024**, *490*, 151568. DOI
 30. Pan, J.; Zhang, Y.; Wang, J.; et al. A quasi-double-layer solid electrolyte with adjustable interphases enabling high-voltage solid-state batteries. *Adv. Mater.* **2022**, *34*, e2107183. DOI
 31. Shi, J.; Nguyen, H.; Chen, Z.; et al. Nanostructured block copolymer single-ion conductors for low-temperature, high-voltage and fast charging lithium-metal batteries. *Energy. Mater.* **2023**, *3*, 300036. DOI
 32. Cho, Y.; Le, M. A.; Hoang, H. A.; Kim, D. Flexible and hyper ion-conductive LATP-embedded semi-interpenetrating polymer network electrolyte membrane for solid-state lithium battery. *J. Energy. Storage.* **2024**, *92*, 112295. DOI
 33. Steinle, D.; Chen, Z.; Nguyen, H.; et al. Single-ion conducting polymer electrolyte for $\text{Li}||\text{LiNi}_{0.6}\text{Mn}_{0.2}\text{Co}_{0.2}\text{O}_2$ batteries - impact of the anodic cutoff voltage and ambient temperature. *J. Solid. State. Electrochem.* **2022**, *26*, 97-102. DOI
 34. Dong, X.; Mayer, A.; Liu, X.; Passerini, S.; Bresser, D. Single-ion conducting multi-block copolymer electrolyte for lithium-metal batteries with high mass loading NCM_{811} cathodes. *ACS. Energy. Lett.* **2023**, *8*, 1114-21. DOI
 35. Dong, X.; Chen, Z.; Gao, X.; et al. Stepwise optimization of single-ion conducting polymer electrolytes for high-performance lithium-metal batteries. *J. Energy. Chem.* **2023**, *80*, 174-81. DOI
 36. Sun, Q.; Wang, S.; Ma, Y.; et al. Li-ion transfer mechanism of gel polymer electrolyte with sole fluoroethylene carbonate solvent. *Adv. Mater.* **2023**, *35*, e2300998. DOI
 37. Mao, M.; Huang, B.; Li, Q.; Wang, C.; He, Y.; Kang, F. In-situ construction of hierarchical cathode electrolyte interphase for high performance $\text{LiNi}_{0.8}\text{Co}_{0.1}\text{Mn}_{0.1}\text{O}_2/\text{Li}$ metal battery. *Nano. Energy.* **2020**, *78*, 105282. DOI
 38. Orue, A.; Arrese-igor, M.; Gonzalez, U.; Gómez, N.; Cid, R.; López-aranguren, P. Enhancing high-voltage solid-state lithium-metal battery performance through a stable solid-electrolyte interphase. *J. Mater. Chem. A.* **2024**, *12*, 22775-84. DOI
 39. Zhao, Q.; Chen, P.; Li, S.; Liu, X.; Archer, L. A. Solid-state polymer electrolytes stabilized by task-specific salt additives. *J. Mater. Chem. A.* **2019**, *7*, 7823-30. DOI
 40. Wang, Z.; Yang, K.; Song, Y.; et al. Polymer matrix mediated solvation of LiNO_3 in carbonate electrolytes for quasi-solid high-voltage lithium metal batteries. *Nano. Res.* **2020**, *13*, 2431-7. DOI
 41. Marangon, V.; Tominaga, Y.; Hassoun, J. An alternative composite polymer electrolyte for high performances lithium battery. *J. Power. Sources.* **2020**, *449*, 227508. DOI
 42. Zhang, X.; Jia, M.; Zhang, Q.; et al. LiNO_3 and TMP enabled high voltage room-temperature solid-state lithium metal battery. *Chem. Eng. J.* **2022**, *448*, 137743. DOI
 43. Wen, S.; Luo, C.; Wang, Q.; et al. Integrated design of ultrathin crosslinked network polymer electrolytes for flexible and stable all-solid-state lithium batteries. *Energy. Storage. Mater.* **2022**, *47*, 453-61. DOI
 44. Zhang, Z.; Cheng, Z.; Qiu, F.; et al. High concentration in situ polymer gel electrolyte for high performance lithium metal batteries. *Chem. Commun.* **2024**, *60*, 6276-9. DOI
 45. Wang, Q.; Ma, Y.; Wang, Y.; et al. In situ catalytic polymerization of LiNO_3 -containing PDOL electrolytes for high-energy quasi-solid-state lithium metal batteries. *Chem. Eng. J.* **2024**, *484*, 149757. DOI
 46. Jing, C.; Dai, K.; Liu, D.; et al. Crosslinked solubilizer enables nitrate-enriched carbonate polymer electrolytes for stable, high-voltage lithium metal batteries. *Sci. Bull.* **2024**, *69*, 209-17. DOI
 47. Cui, Z.; Hassoun, J.; Tominaga, Y. Development of polycarbonate-based electrolytes with in situ polymerized electrolyte interlayers for lithium-metal batteries. *J. Energy. Storage.* **2024**, *79*, 110175. DOI
 48. Li, P.; Zhang, H.; Lu, J.; Li, G. Low concentration sulfolane-based electrolyte for high voltage lithium metal batteries. *Angew. Chem. Int. Ed.* **2023**, *62*, e202216312. DOI
 49. Zhao, C.; Lu, Y.; Yan, K.; et al. Tailoring the chemical/electrochemical response in a quasi-solid polymer electrolyte enables the simultaneous in situ construction of superior cathodic and anodic interfaces. *Adv. Energy. Mater.* **2024**, *14*, 2304532. DOI
 50. Wang, Y.; Li, T.; Yang, X.; et al. 2D solid-electrolyte interphase built by high-concentration polymer electrolyte for highly reversible silicon anodes. *Adv. Energy. Mater.* **2024**, *14*, 2303189. DOI
 51. Ren, W.; Luo, C.; Huang, Y.; et al. Hydroxypropylmethylcellulose: functional material carrier for in-situ solid electrolyte engineering of advanced lithium metal batteries. *Energy. Storage. Mater.* **2023**, *59*, 102777. DOI
 52. Li, B.; Chao, Y.; Li, M.; et al. A review of solid electrolyte interphase (SEI) and dendrite formation in lithium batteries. *Electrochem. Energy. Rev.* **2023**, *6*, 147. DOI
 53. Wang, X.; Xu, L.; Li, M.; et al. LiNO_3 regulated rigid-flexible-synergistic polymer electrolyte boosting high-performance Li metal batteries. *Energy. Storage. Mater.* **2024**, *73*, 103778. DOI
 54. Cui, Z.; Marangon, V.; Hassoun, J.; Tominaga, Y. Polycarbonate-based composite polymer electrolytes with Al_2O_3 enhanced by in situ polymerized electrolyte interlayers for all-solid-state lithium-metal batteries. *J. Power. Sources.* **2024**, *611*, 234760. DOI
 55. Watanabe, M. Estimation of Li^+ transport number in polymer electrolytes by the combination of complex impedance and potentiostatic polarization measurements. *Solid. State. Ion.* **1988**, *28-30*, 911-7. DOI
 56. Adams, B. D.; Zheng, J.; Ren, X.; Xu, W.; Zhang, J. Accurate determination of coulombic efficiency for lithium metal anodes and lithium metal batteries. *Adv. Energy. Mater.* **2018**, *8*, 1702097. DOI
 57. Seah, M. P. Simple universal curve for the energy-dependent electron attenuation length for all materials. *Surf. Interface. Anal.* **2012**, *44*, 1353-9. DOI

58. Fairley, N.; Fernandez, V.; Richard-plouet, M.; et al. Systematic and collaborative approach to problem solving using X-ray photoelectron spectroscopy. *App. Surf. Sci. Adv.* **2021**, *5*, 100112. [DOI](#)
59. Jagger, B.; Pasta, M. Solid electrolyte interphases in lithium metal batteries. *Joule* **2023**, *7*, 2228-44. [DOI](#)
60. Orue, A.; Arrese-Igor, M.; Cid, R.; et al. High resolution XPS of organic polymers: the scienta ESCA300 database (Beamson, G.; Briggs, D.). *J. Chem. Educ.* **1993**, *70*, A25. [DOI](#)
61. Orue, A.; Arrese-igor, M.; Cid, R.; et al. Enhancing the polymer electrolyte-Li metal interface on high-voltage solid-state batteries with Li-based additives inspired by the surface chemistry of $\text{Li}_7\text{La}_3\text{Zr}_2\text{O}_{12}$. *J. Mater. Chem. A* **2022**, *10*, 2352-61. [DOI](#)
62. Xue, W.; Shi, Z.; Huang, M.; et al. FSI-inspired solvent and “full fluorosulfonyl” electrolyte for 4 V class lithium-metal batteries. *Energy Environ. Sci.* **2020**, *13*, 212-20. [DOI](#)
63. Wurster, V.; Engel, C.; Graebe, H.; Ferber, T.; Jaegermann, W.; Hausbrand, R. Characterization of the interfaces in $\text{LiFePO}_4/\text{PEO-LiTFSI}$ composite cathodes and to the adjacent layers. *J. Electrochem. Soc.* **2019**, *166*, A5410-20. [DOI](#)
64. Liu, Y.; Yang, T.; Fang, R.; et al. Ultra-homogeneous dense Ag nano layer enables long lifespan solid-state lithium metal batteries. *J. Energy Chem.* **2024**, *96*, 110-9. [DOI](#)
65. Seki, S.; Kobayashi, Y.; Miyashiro, H.; Mita, Y.; Iwahori, T. Fabrication of high-voltage, high-capacity all-solid-state lithium polymer secondary batteries by application of the polymer electrolyte/inorganic electrolyte composite concept. *Chem. Mater.* **2005**, *17*, 2041-5. [DOI](#)
66. Sabet P, Sauer DU. Separation of predominant processes in electrochemical impedance spectra of lithium-ion batteries with nickel-manganese-cobalt cathodes. *J. Power. Sources.* **2019**, *425*, 121-9. [DOI](#)
67. Charbonneau, V.; Lasia, A.; Brisard, G. Impedance studies of Li^+ diffusion in nickel manganese cobalt oxide (NMC) during charge/discharge cycles. *J. Electroanal. Chem.* **2020**, *875*, 113944. [DOI](#)
68. Pritzl, D.; Bumberger, A. E.; Wetjen, M.; Landesfeind, J.; Solchenbach, S.; Gasteiger, H. A. Identifying contact resistances in high-voltage cathodes by impedance spectroscopy. *J. Electrochem. Soc.* **2019**, *166*, A582-90. [DOI](#)
69. Brug, G.; van, E. A.; Sluyters-Rehbach, M.; Sluyters, J. The analysis of electrode impedances complicated by the presence of a constant phase element. *J. Electroanal. Chem. Interfacial. Electrochem.* **1984**, *176*, 275-95. [DOI](#)
70. Cabañero, M. M. A.; Boaretto, N.; Naylor, A. J.; et al. Are polymer-based electrolytes ready for high-voltage lithium battery applications? An overview of degradation mechanisms and battery performance. *Adv. Energy Mater.* **2022**, *12*, 2201264. [DOI](#)
71. Boaretto, N.; Garbayo, I.; Valiyaveetil-Sobhanraj, S.; et al. Lithium solid-state batteries: state-of-the-art and challenges for materials, interfaces and processing. *J. Power. Sources.* **2021**, *502*, 229919. [DOI](#)
72. Chiou, M.; Borzutzki, K.; Thienenkamp, J. H.; et al. Durable fast-charging lithium metal batteries designed with cross-linked polymer electrolytes and niobate-coated cathode. *J. Power. Sources.* **2022**, *538*, 231528. [DOI](#)
73. Chen, Y.; Lennartz, P.; Liu, K. L.; et al. Towards all-solid-state polymer batteries: going beyond PEO with hybrid concepts. *Adv. Funct. Mater.* **2023**, *33*, 2300501. [DOI](#)
74. Zhai, P.; Qu, S.; Ahmad, N.; Hua, Z.; Shao, R.; Yang, W. Constructing nano-interlayer inhibiting interfacial degradation toward high-voltage PEO-based all-solid-state lithium batteries. *Small* **2024**, *20*, e2310547. [DOI](#) [PubMed](#)
75. Zhang, W.; Lu, Y.; Wan, L.; et al. Engineering a passivating electric double layer for high performance lithium metal batteries. *Nat. Commun.* **2022**, *13*, 2029. [DOI](#) [PubMed](#) [PMC](#)
76. Jin, C.; Huang, Y.; Li, L.; et al. A corrosion inhibiting layer to tackle the irreversible lithium loss in lithium metal batteries. *Nat. Commun.* **2023**, *14*, 8269. [DOI](#) [PubMed](#) [PMC](#)
77. Ma, M.; Guo, X.; Wen, P.; et al. Reactive solid polymer layer: from a single fluoropolymer to divergent fluorinated interface. *Angew. Chem. Int. Ed.* **2024**, *63*, e202407304. [DOI](#)